NAVAL POSTGRADUATE SCHOOL

MONTEREY, CALIFORNIA

THESIS

PREDICTING SOIL STRENGTH WITH REMOTE SENSING DATA

by

Jon T. Wende

September 2010

| Thesis Co-Advisors: | R. C. Olsen |
| | C. Bachmann |

Approved for public release; distribution is unlimited

THIS PAGE INTENTIONALLY LEFT BLANK

REPORT DOCUMENTATION PAGE		*Form Approved OMB No. 0704-0188*

Public reporting burden for this collection of information is estimated to average 1 hour per response, including the time for reviewing instruction, searching existing data sources, gathering and maintaining the data needed, and completing and reviewing the collection of information. Send comments regarding this burden estimate or any other aspect of this collection of information, including suggestions for reducing this burden, to Washington headquarters Services, Directorate for Information Operations and Reports, 1215 Jefferson Davis Highway, Suite 1204, Arlington, VA 22202-4302, and to the Office of Management and Budget, Paperwork Reduction Project (0704-0188) Washington DC 20503.

1. AGENCY USE ONLY *(Leave blank)*	2. REPORT DATE September 2010	3. REPORT TYPE AND DATES COVERED Master's Thesis
4. TITLE AND SUBTITLE Predicting Soil Strength with Remote Sensing Data		5. FUNDING NUMBERS
6. AUTHOR(S) Jon T. Wende		

7. PERFORMING ORGANIZATION NAME(S) AND ADDRESS(ES)
   Naval Postgraduate School
   Monterey, CA 93943-5000
		8. PERFORMING ORGANIZATION REPORT NUMBER

9. SPONSORING /MONITORING AGENCY NAME(S) AND ADDRESS(ES)
   Naval Research Laboratory (Code 7232)
   4555 Overlook Ave, SW
   Washington, DC 20375
		10. SPONSORING/MONITORING AGENCY REPORT NUMBER

11. SUPPLEMENTARY NOTES The views expressed in this thesis are those of the author and do not reflect the official policy or position of the Department of Defense or the U.S. Government. IRB Protocol number _____.

12a. DISTRIBUTION / AVAILABILITY STATEMENT Approved for public release; distribution is unlimited	12b. DISTRIBUTION CODE A

13. ABSTRACT (maximum 200 words)

Predicting soil strength from hyperspecral imagery enables amphibious planners to determine trafficability in the littorals. Trafficability maps can then be generated and used during the intelligence preparation of the battlespace allowing amphibious planners to select a suitable landing zone. In February and March 2010, the Naval Research Laboratory sponsored a multi-sensor remote sensing and field calibration and field validation campaign (CNMI'10). The team traveled to the islands of Pagan, Tinian, and Guam located in the Marianas archipelago. Airborne hyperspectral imagery along with ground truth data was collected from shallow water lagoons, beachfronts, vegetation, and anomalies such as World War II relics.

In this thesis, beachfront hyperspectral data obtained on site was used as a reference library for evaluation against airborne hyperspectral data and ground truth data in order to determine soil strength for creating trafficability maps. Evaluation of the airborne hyperspectral images was accomplished by comparing the reference library spectra to the airborne images. The spectral angle between the reference library and airborne images was calculated producing the trafficability maps amphibious planners can use during the intelligence preparation of the battlespace.

14. SUBJECT TERMS Hyperspectral, Littoral, Amphibious Landing, Trafficability, HyMap, Hy Vista, Commonwealth of the Northern Mariana.	15. NUMBER OF PAGES 95
	16. PRICE CODE

17. SECURITY CLASSIFICATION OF REPORT Unclassified	18. SECURITY CLASSIFICATION OF THIS PAGE Unclassified	19. SECURITY CLASSIFICATION OF ABSTRACT Unclassified	20. LIMITATION OF ABSTRACT UU

NSN 7540-01-280-5500

Standard Form 298 (Rev. 2-89)
Prescribed by ANSI Std. 239-18

THIS PAGE INTENTIONALLY LEFT BLANK

PREDICTING SOIL STRENGTH WITH REMOTE SENSING DATA

Jon T. Wende
Lieutenant, United States Navy
B.S., Old Dominion University, 2006

Submitted in partial fulfillment of the
requirements for the degree of

MASTER OF SCIENCE IN SPACE SYSTEMS OPERATIONS

from the

NAVAL POSTGRADUATE SCHOOL
September 2010

Author: Jon T. Wende

Approved by: R. C. Olsen
                 Thesis Co-Advisor

                 C. Bachmann
                 Thesis Co-Advisor

                 Rudolf Panholzer
                 Chair, Space Systems Academic Group

THIS PAGE INTENTIONALLY LEFT BLANK

ABSTRACT

Predicting soil strength from hyperspecral imagery enables amphibious planners to determine trafficability in the littorals. Trafficability maps can then be generated and used during the intelligence preparation of the battlespace allowing amphibious planners to select a suitable landing zone. In February and March 2010, the Naval Research Laboratory sponsored a multi-sensor remote sensing and field calibration and field validation campaign (CNMI'10). The team traveled to the islands of Pagan, Tinian, and Guam located in the Marianas archipelago. Airborne hyperspectral imagery along with ground truth data was collected from shallow water lagoons, beachfronts, vegetation, and anomalies such as World War II relics.

In this thesis, beachfront hyperspectral data obtained on site was used as a reference library for evaluation against airborne hyperspectral data and ground truth data in order to determine soil strength for creating trafficability maps. Evaluation of the airborne hyperspectral images was accomplished by comparing the reference library spectra to the airborne images. The spectral angle between the reference library and airborne images was calculated producing the trafficability maps amphibious planners can use during the intelligence preparation of the battlespace.

THIS PAGE INTENTIONALLY LEFT BLANK

TABLE OF CONTENTS

THIS PAGE INTENTIONALLY LEFT BLANK

LIST OF FIGURES

x

LIST OF TABLES

THIS PAGE INTENTIONALLY LEFT BLANK

LIST OF ACRONYMS AND ABBREVIATIONS

AFRL	Air Force Research Laboratory
AIS	Airborne Imaging Spectrometer
ASD	Analytical Spectral Devices
AVRIS	Airborne Visible/Infrared Imaging Spectrometer
BEACHREP	Beach Report
CBR	California Bearing Ratio
CNMI	Commonwealth of the Northern Mariana Islands
DARPA	Defense Advanced Research Projects Agency
DCP	Dynamic Cone Penetrometer
DN	Digital Number
DPI	DCP Penetration Index
ENVI	Environment for Visualizing Images
GEOINT	Geographical Intelligence
GIS	Geographic Information System
GPS	Global Positioning System
HQMC	Head Quarters Marine Corps
HSI	Hyperspectral Imagery
HYDICE	Hyperspectral Digital Imagery Collection Experiment
IDL	Interactive Data Language
IPB	Intelligence Preparation of the Battlespace
IR	Intelligence Requirements
JPL	Jet Propulsion Laboratory
LWD	Lightweight Deflectometer
MARFORPAC	Marine Corps Forces Pacific
MCWP	Marine Corps Warfighting Publication
MEF	Marine Expeditionary Force
MIRC	Marine Information Resources Corporation
NASA	National Aeronautics and Space Administration
NOAA	National Oceanic and Atmospheric Administration
NPS	Naval Postgraduate School
NRL	Naval Research Laboratory
ONR	Office of Naval Research
SAM	Spectrum Angle Mapper
SMIFTS	Spatially Modulated Imaging Fourier Transform Spectrometer
SWIR	Short-wave Infrared
TAFKAA	The Algorithm Formerly Known As Atmospheric Removal
TOPSET	Topographic Set

US	United States
USDA	United States Department of Agriculture
USMC	United States Marine Corps
VNIR	Visible/Near Infrared

ACKNOWLEDGMENTS

I would like to thank Dr. Richard C. Olsen, Director of the Naval Postgraduate Remote Sensing Center, and Dr. Charles M. Bachmann, Naval Research Laboratory Remote Sensing Division, for their guidance and support during the development of this thesis. It was truly a tremendous opportunity and memorable experience to work with Dr. Bachmann and his team throughout the course of the experiment. Their dedication and professionalism were remarkable. Additionally, I would like to thank Professor Olsen's staff of Ms. Krista Lee, Ms. Angela Kim, and Ms. Arwin Ross for their tremendous assistance. Their guidance was invaluable and very much appreciated.

Furthermore, I would like to thank my loving wife, Michele, and my children for their love and support. They are my foundation and without them, none of this would be possible.

THIS PAGE INTENTIONALLY LEFT BLANK

I. INTRODUCTION

A. TRAFFICABILITY AND SOIL STRENGTH

The *Marine Corps Vision and Strategy* estimates that by 2025, the world's population will increase by thirty percent with a large percentage heavily concentrated near the littorals. Additionally, the effects from climate changes may cause an increased number of natural disasters in those regions and with the vast majority of the population living near the coastal regions, social instability is a serious concern.   Where there is social instability, there are extremist or criminal groups looking to exploit the region. These challenges are real and the United States (U.S.) must be able to operate in the littoral in order to deal with them. For instance, from the end of the Cold War until 2009, U.S. amphibious forces have responded to at least 104 crises, see Figure 1 (USMC, 2009). Geographic combatant commanders' have a need for amphibious forces capable of conducting security cooperation, regional deterrance, and crisis response (USMC, 2009).
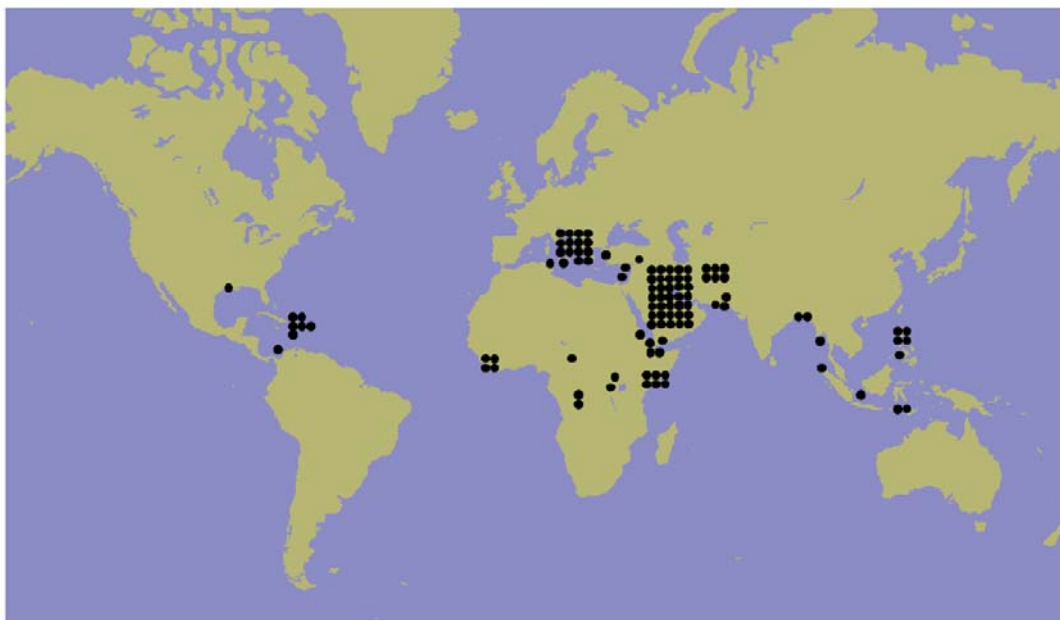
Figure 1.   Post-Cold War U.S. Amphibious Responses to Crises (From Amphibious Ops in 21st century, 2009)

Hyperspectral imagery (HSI) is a versatile technology that enables combatant commanders to properly plan amphibious operations. It is one of many tools commanders can use to gather intelligence about the littoral operational area during planning and prior to the execution of any amphibious operations. Understanding geographical obstacles a landing force may encounter at or near the landing zone, knowing possible locations of enemy resistance, or identifying enemy target locations prior to executing the operation not only contributes to mission success, but it also saves lives. The commander uses the HSI in his or her intelligence estimate, and that intelligence is then expressed graphically during the intelligence preparation of the battlespace (IPB).

This thesis analyzes the field data collected from an experiment conducted from February through March 2010 on the islands of Pagan, Tinian, and Guam, (located in the Commonwealth of the Northern Mariana Islands (CNMI)). Ground truth data was gathered from each location and was used for correlation against HSI data obtained from both ground and airborne hyperspectral sensors. Knowing the exact locations and spectral signatures of underwater obstacles, landing zone soil content, enemy bunker locations, and enemy aircrafts obtained in the field will assist in the identification of these objects when analyzing the hyperspectral data. Additionally, this contribution to an expanding spectral library of a wide range of spectral signatures from various locations around the world enhances the ability to identify objects from HSI alone in the event the ground truth data is not obtainable.

II.   BACKGROUND AND HISTORY

A.   REMOTE SENSING

Remote sensing is the practice of examining features as observed in several regions of the electromagnetic spectrum (Campbell, 1996). Hyperspectral remote sensing is based on examining many narrowly defined spectral channels vice several broadly defined spectral regions. Visible/Near Infrared (VNIR) to Short-wave Infrared (SWIR) sensors can consist of several hundred channels, each of which is only five to ten nanometers wide. Instruments used in spectroscopy collect radiation and divide it into spectral regions. This allows the bands to be measured electronically. The detailed examination of accurate spectral data, referred to as spectroscopy, allows for the identification of features such as biological and geological phenomena or self-correction of data in some bands of data using information from other bands possible (Campbell, 1996).

B.   HYPERSPECTRAL REMOTE SENSING

Hyperspectral remote sensing is the application of spectroscopy in which one examines very detailed spectra for images of the earth's surface, applies corrections for atmospheric effects, and then matches them to spectra of known libraries. The known libraries in the context of this thesis are the ground sample spectra obtained from the islands of Pagan, Tinian, and Guam. Several data points, to include: ground, bunker, various foliage types, white and black calibration panels, and old World War II Japanese aircrafts, were measured for their spectral signatures and each position was accurately marked via the global positioning system (GPS). Identification within the hyperspectral image can be correlated to the actual known location and spectral signature of each data point.

C.   EARLY IMAGING SPECTROMETERS

In the early 1980s, the Jet Propulsion Laboratory (JPL) designed one of the world's first hyperspectral sensors known as the Airborne Imaging Spectrometer (AIS)

(Campbell, 1996). The AIS collected spectra in 128 bands, each with a spectral resolution of ten nanometers and a spatial resolution of eight meters. The follow-on airborne sensor to AIS, known as Airborne Visible/Infrared Imaging Spectrometer (AVIRIS), was developed in 1987 by the National Aeronautics and Space Administration (NASA) JPL. AVIRIS collected spectra from 400 nanometers to 2500 nanometers using 224 spectral channels, each ten nanometers wide with a spatial resolution of about twenty meters (Anderson, et al., 1994). The success of AVIRIS lead to the development of the Hyperspectral Digital Imagery Collection Experiment, HYDICE, which also covered spectra bands from 400 nanometers to 2500 nanometers. HYDICE had a higher signal-to-noise ratio (SNR) and better spatial and spectral resolution and radiometric accuracy than AVIRIS. An even more advanced spectrometer developed by the Defense Advanced Research Projects Agency (DARPA), the Office of Naval Research (ONR), and the University of Hawaii, was the Spatially Modulated Imaging Fourier Transform Spectrometer (SMIFTS). This system contains 100 spectral bands between 1000 nanometers to 2500 nanometers. The high spectral resolution, large number of spectral bands, high spatial resolution, and longer dwell times all result from an availability of two-dimensional focal planes (Anderson, et al., 1994). Both HYDICE and SMIFTS were the beginning of the state-of-the-art in hyperspectral imaging but many more are available today. The CNMI'10 experiment collected hyperspectral data from the HyVista HYMAP and the Naval Research Laboratory's (NRL) microSHINE sensors, which are described in further detail in Chapter III.

D. PREVIOUS CAMPAIGNS

In 2009, Marine Corps Captain Chris Jones completed his thesis work at the Naval Postgraduate School (NPS) using data gathered from the Shoalwater Bay Training Area in Queensland, Australia. Similar to the CNMI'10 campaign, the Australia campaign used ground truth data for correlation against HSI data to create trafficability maps. His trafficability map results can be seen in Figure 2. This map indicates the beachfront region, depicted mostly in yellow, blue, and green, will be moderately suitable for trafficability. Captain Jones was able to validate this prediction with the ground truth data collected throughout his experiment. The CNMI'10 campaign gathered ground truth

data from three islands in the Mariana archipelago to be used for validation against HSI data collected from each location. This experiment will be discussed in further detail in Chapter IV.
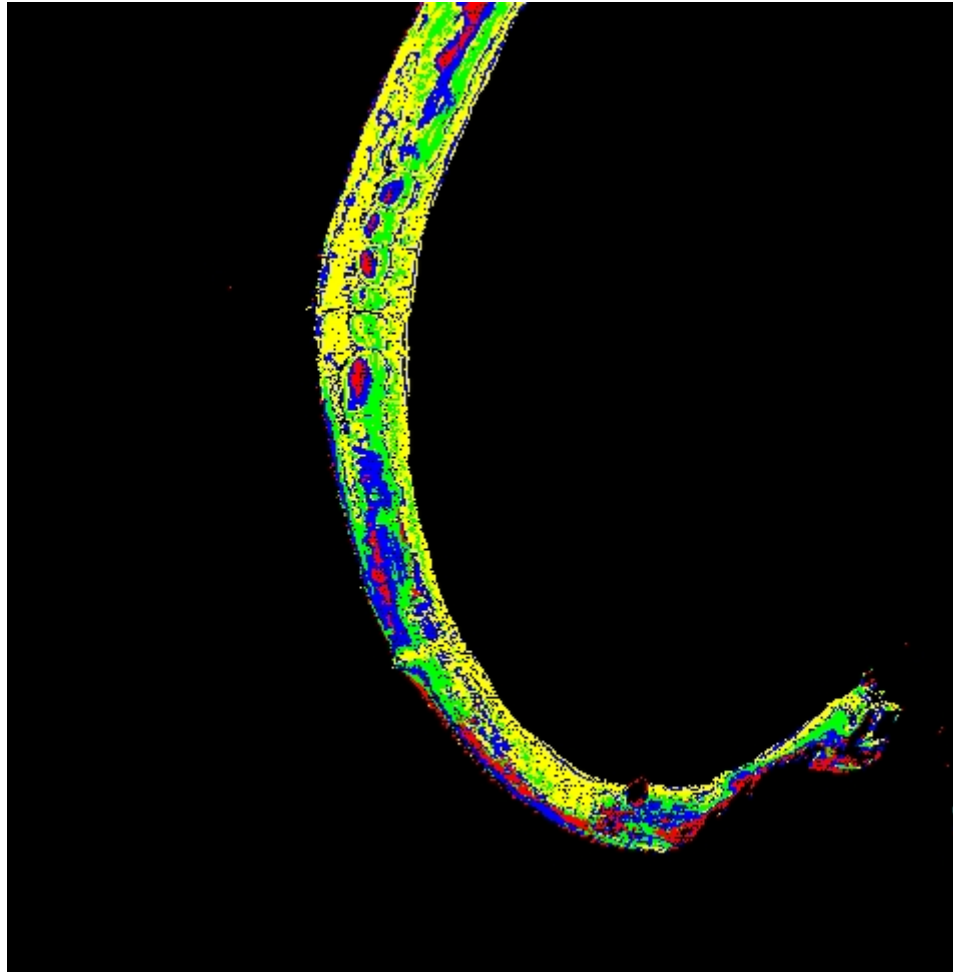

Figure 2. Trafficability Results from Captain Chris Jones' Thesis

THIS PAGE INTENTIONALLY LEFT BLANK

III. SOIL ENGINEERING

A. INTRODUCTION

Determining the substrate bearing strength depends on several factors, such as soil type, the soil grain size and its distribution, the amount of moisture present in the soil, and the depth of the each layer (Bachmann, C. M., et al., 2007). HSI reveals the soil type, grain sizes, and moisture content, which are some of the data necessary to determine soil strength. However, this is limited to the surface. How useful is HSI for indicating potential bearing strength? Since retrieval of soil content is not always an option, this thesis attempts to show that data obtained from HSI can be used to estimate, with a large degree of accuracy, the substrate bearing strength. Ground truth data obtained in the CNMI'10 experiment will be used to determine the correlation to the HSI data. Then, a map can be created where similar spectra within the image will be matched to those of known soil strengths.

B. PHYSICAL PROPERTIES OF SOIL

1. Soil Type

Just as the human eye discriminates colors based upon wavelength-dependent scattering of visible-light photons, HSI has the ability to discriminate soil types. As examples, the region around 0.85-0.92µm exhibits the absorption bands associated with iron oxides, often referred to as limonite, while 1.0-3.0µm provides additional information, most notably rocks that reflect the strongest around 1.6µm (Goetz et al., 1981). Vegetation's reflectance in the visible and near-infrared regions differs substantially from that of rocks and soils and can alter the reflectance signatures of the rocks and minerals beneath. Furthermore, the discrimination of vegetation apart from the soil type can be used as an indirect indicator of the composition of the soil beneath (Goetz et al., 1981). Knowing whether the soil beneath is primarily iron or quartz along

with being able to determine presence or absence of vegetation leads directly to understanding how strong the substrate is. HSI provides the necessary reflectance data to determine the soil type.

2.   Grain Size and Distribution

Size classification of soil particles is measured in millimeters and various agencies propose different thresholds, all of which are fairly similar. A table of the United States Department of Agriculture's (USDA) limits is listed in Table 1.

	Gravel	Very Coarse Sand	Coarse Sand	Medium Sand	Fine Sand	Very Fine Sand	Silt Size	Clay Size	Colloidal Size
USDA	>2	2.0-1.0	1.0-0.5	0.5-0.25	0.25-0.10	0.10-0.05	0.05-0.002	< 0.002	___

Table 1.   Size Classification of Soil Particles (in mm) (From Soil Engineering, 1960)

The density of soil is greater when it consists of particles of various sizes, rather than particles of uniform size (Spangler, 1960). This is based on the fact that smaller particles will fall into the void spaces between larger particles, thus increasing the volume of the solid material. The distribution of particle sizes throughout soil is known as the grading, and falls into ten commonly used textural classes, see Table 2.

Textural Class	Composition in %		
	Sand	Silt-size	Clay-size
Sand	80-100	0-20	0-20
Sandy loam	50-80	0-50	0-20
Loam	30-50	30-50	0-20
Silt loam	0-50	50-100	0-20

Sandy clay loam	50-80	0-30	20-30
Clay loam	20-50	20-50	20-30
Silty clay loam	0-30	50-80	20-30
Sandy clay	55-70	0-15	30-45
Silty clay	0-15	55-70	30-45
Clay	0-55	0-55	30-100

Table 2.   Textural Classification of Soil Based on Grading (From Soil Engineering, 1960)

Another method for determining textural classes can be done by using a triangular chart, see Figure 3. For example, assume 30% sand, 40% silt, and 30% clay. Follow the triangle on the sand side to 30% and follow the line extending upward to the left until it intersects with the line extending downward and to the right from 30% clay, or downward to the left from 40% silt. Either way, the lines will intersect at clay loam and this represents the classification of that particular sample.
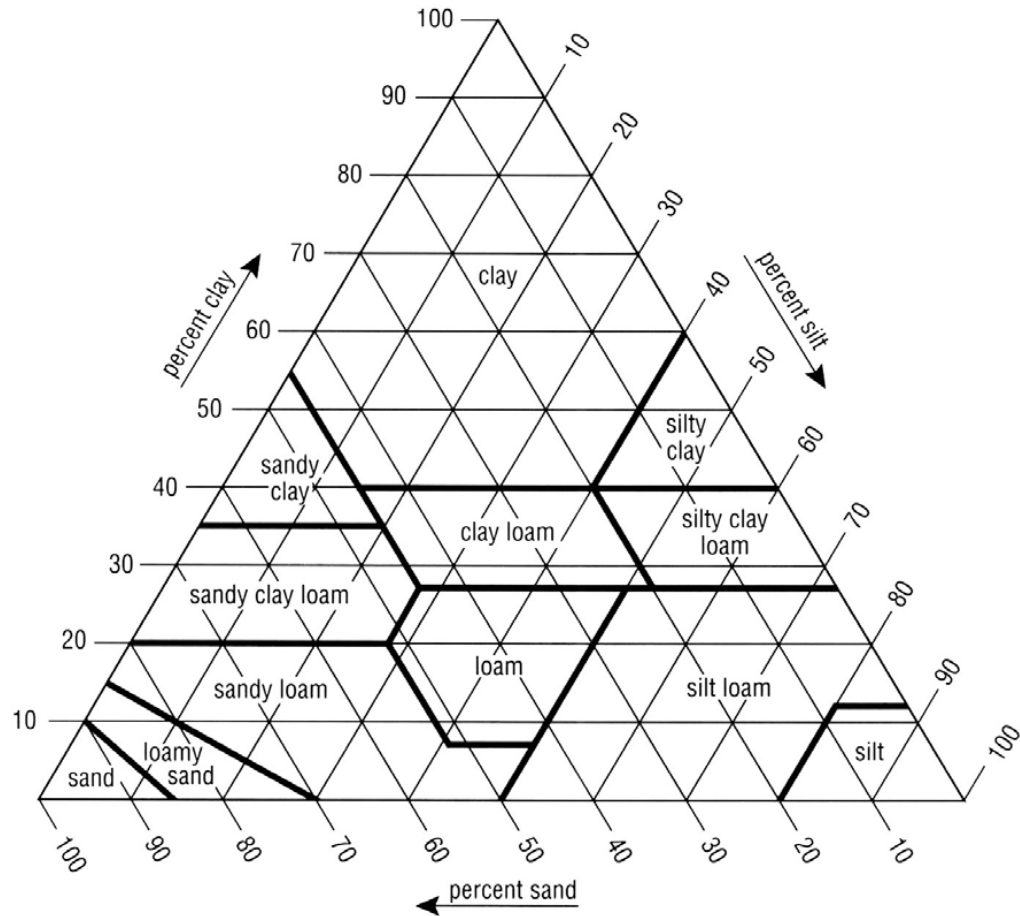
Figure 3.   Textural Classification Chart (From Soil Engineering, 1960)

The soil samples collected in this experiment were separated into various sizes by shaking them through a nest of sieves, each one having a different size of mesh ranging from 25mm to 25µm. Each particle-size group was weighed to determine how much of each grain size was in the sample, see Figure 4. From this, a particle-size distribution curve can be made. This curve can then be compared against other soil measurements to determine how soil size and distribution factor into soil strength.

Figure 4.   Sieves and separated soil samples

This type of analysis of the soil is considered a mechanical analysis. While HSI is unable to provide any data about the distribution of particles throughout the soil, some studies have shown HSI has the ability to discriminate soil grain size (Ghrefat, et al., 2007). A table can then be created to illustrate how grain size and distribution correlates to a HSI spectral signature. Then, in situations where only spectra can be gathered, this correlation can then be used to estimate the soil strength.

3.   Moisture Content

The effect moisture has on soil is a matter of common knowledge to nearly everyone who stops to give it consideration. For instance, after the rainy season in various locations around the world, numerous mudslides and cave-ins occur and cars have difficulty driving on muddy surfaces. The increased moisture content in the soil reduces the soils ability to resist shearing stresses and also weakens its bearing capacity (Spangler, 1960). However, walking on the beach is much easier when walking closer to

the water's edge versus walking on dry sand. While water in the ladder example affects the soil differently than the first example, it is clear that water greatly influences the behavior of the soil.

Previous experiments conducted by Dr. Bachmann revealed that the presence or absence of moisture was one of two factors greatly affecting the bearing capacity in beach regions (Bachmann, et al., 2007). While water does affect soils differently, this thesis is focused on how the water content contributes to the strength of the soil. Each soil sample collected during CNMI'10 was weighed in its natural state and then dried in a microwave oven and reweighed. The resulting dry weight versus wet weight determines the moisture content. Results from the CNMI'10 experiment will be discussed in a later section.

C. EQUIPMENT USED FOR DETERMINING SOIL STRENGTH

1. Dynamic Cone Penetrometer

The Dynamic Cone Penetrometer (DCP) is a device used for measuring the strength of in situ soil and the thickness and location of underlying soil layers (Kessler, 2007). It consists of two 16mm diameter shafts connected at the mid-point. The lower portion contains an anvil and a 30 or 60 degree pointed tip, depending on soil stiffness, which is driven into the soil by dropping a sliding 10 pound hammer from the upper portion onto the anvil.
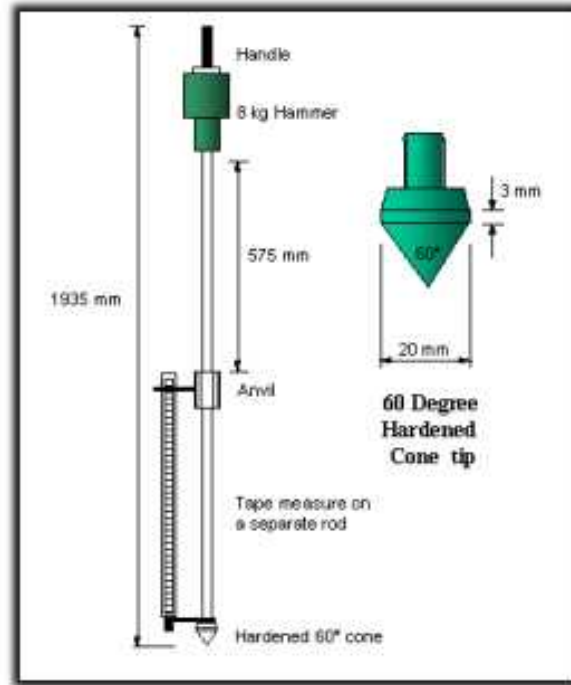
Figure 5.   Dynamic Cone Penetrometer (From DCP Users Guide, 2007)

The amount of the penetration, in millimeters, from each drop of the hammer is recorded and is known as the DCP penetration index (DPI). This DPI can then be plotted versus depth to identify thicknesses and strengths, and it can then be correlated to the soil parameter referred to as the California Bearing Ratio (CBR). CBR is expressed as a percentage and is equal to the measured pressure for site soils [N/mm^2] versus the pressure to achieve equal penetration on standard soil [N/mm^2]. Converting DPI into CBR is done using the expression:

$$log\ CBR = 2.46 - 1.12logDPI$$

or

$$CBR = 10^{2.46\ -\ 1.12logDPI}$$

where DPI is expressed in mm/blow. A higher CBR correlates to harder soils as is indicated by the reduced penetration per blow from the DCP. When feasible, DCP measurements were conducted at each data location throughout the CNMI'10 campaign.

Correlation Plot of CBR vs. DPI
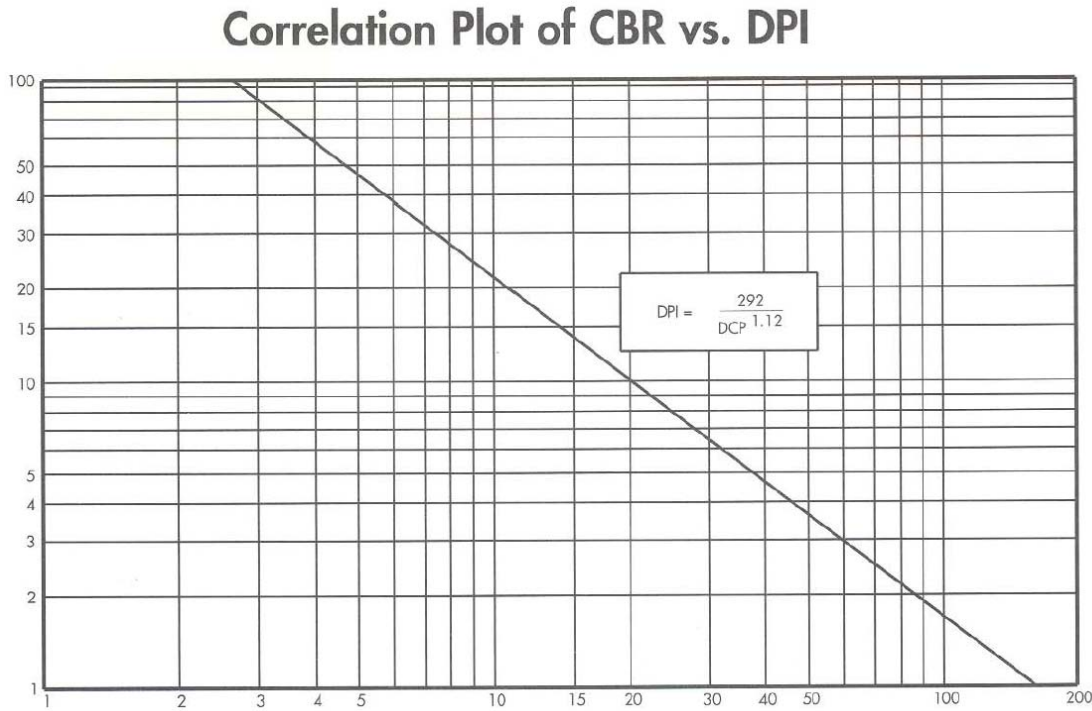
$$DPI = \frac{292}{DCP^{1.12}}$$

Figure 6.   CBR(%) versus DPI(mm/blow) (From DCP Users Guide, 2007, DPI = $292/DCP^{1.12}$)

2.   Lightweight Deflectometer

The Lightweight Deflectometer (LWD) is a device used to evaluate the dynamic deflection modulus, Evd, in MN/m^2. This modulus is an index of the bearing capacity on subgrade, subsoil, granular layers made of unbound aggregates or recycled materials, backfilling materials, soil stabilization with lime and earth-roads (Zorn, 2005). It operates by generating a pulse from a falling mass from a preset height that is dropped onto a system that transmits the load pulse through a plate resting on the surface to be tested. The resulting vertical surface deflection is measured by the portable data processing and storage system and the peak deflection from the force pulse at each location is recorded. This data is repeated three times and results can be printed on site.

14

Figure 7 shows a drawing of a LWD and an example of a printout. The larger the Evd value corresponds to a harder surface. The values seen during the experiment ranged from 1.2-199.1MN/m^2 with an average Evd of 12.5MN/m^2. When feasible, LWD measurements were conducted and the results are analyzed later on in this thesis.

(1) grip
(2) top fix and release mechanism
(3) guide rod
(4) round grip
(5) 10 or 15 kg - falling weight
(6) lock pin
(7) set of steel springs
(8) anti tipping fixture
(9) load centre ball
(10) carry grip
(11) loading plate
(12) socket for the connection to the electronic device
(13) adapter plate
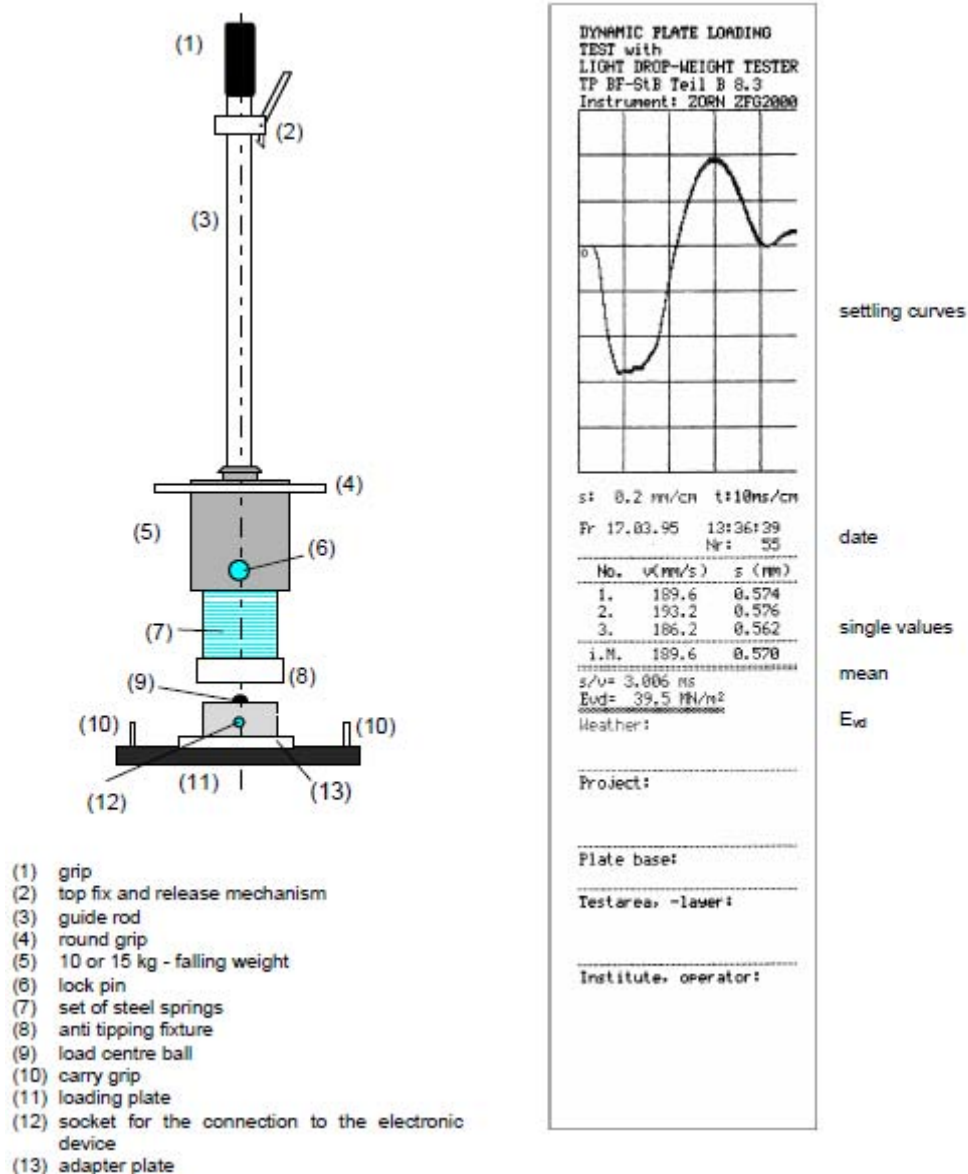
Figure 7.   Left (LWD)/Right (LWD Printout) (From LWD Users Guide, 2005)

D. SPECTRAL EQUIPMENT USED DURING EXPERIMENT

The CNMI'10 experiment required data collection from several pieces of equipment in addition to those described above and are discussed in further detail below.

1. Airborne Hyperspectral

Hyperspectral imagers HyMAP and the NRL's microSHINE were flown on board a dual-port Piper Navajo aircraft to gather images throughout the experiment. Efforts were made to obtain images at both high and low tide to include the surrounding waters at the selected sites. Additionally, the Pagan and Guam images captured two 10 x 10 meter tarps, one white and one black, for sensor calibration.

Figure 8.   White Calibration Panel (Pagan)

a.   HyVista HYMAP

Integrated Spectronics, Sydney, Australia, developed the Hyperspectral Mapper (HYMAP) in the late 1990s for applications such as geological mapping and mineral exploration, see Figure 9.

Figure 9.   HYMAP

Current sensors contain 128 bands covering 0.44-2.5µm and have achieved high levels of performance in terms of SNR, band to band registration and image quality (Cocks, et al., 1998). The sensor is mounted on a three-axis, gyro-stabilized platform and contains an optomechanically scanned system incorporating spectrographic/detector array modules, on-board reference lamp and a shutter synchronized to scan line readouts for dark current monitoring (Cocks, et al., 1998). The 128 band spectral range of the sensor is divided into four 32-element detector arrays, see Table 3. The HYMAP sensor was mounted onboard a Piper Navajo aircraft, see Figure 10. The aircraft was flown above all three experiment locations at an altitude of ~10,000 feet while the science team collected ground truth data.

Spectral Configuration			
Module	Spectral Range	Bandwidth Across Module	Average Spectral Sampling Interval
VIS	0.45-0.89µm	15-16nm	15nm
NIR	0.89-1.35µm	15-16nm	15nm
SWIR1	1.40-1.80µm	15-16nm	13nm
SWIR2	1.95-2.48µm	18-20nm	17nm

Table 3.   HYMAP Sensor Characteristics (From Cocks et al., 1998)

Figure 10.   Piper Aircraft used during CNMI'10

b.   *NRL MicroSHINE*

The Naval Research Laboratory sensor microSHIINE is a visible and near infrared (VNIR) hyperspectral sensor that operates from 0.38-1.0 microns (Bachmann, et al., 2010). Data were collected from this sensor, but atmospheric corrections problems have made data analysis with the microSHINE data difficult. This thesis does not analyze data from microSHINE, as efforts to correct the data are still being made.

2.   FieldSpec Pro Spectroradiometer

Analytical Spectral Devices (ASD) Incorporated designs and builds instruments used in the field of spectrometry. In the CNMI'10 experiment, the instrument of choice was the field-portable Full Range FieldSpec Pro, which measures light energy from 350-2500nm. The research teams, and this thesis, refer to this device as the ASD. The team had three ASDs on hand throughout the experiment. One ASD was continually sampling a spectrally flat (Lambertian) Spectralon white reference plaque when the other ASD's were in use collecting spectra. The reference plaque provides a reflectance of a known material that has approximately 100% reflectance across the entire spectrum and is used to remove the characteristics of the illumination source. The other two ASDs were used to take field measurements from various spectra such as soil samples, foliage, bunkers, aircrafts, calibration panels, lava rocks, and shallow-water bathymetry. Basic theory of operation is the ASD collects light, via fiber optics, and then projects the light onto a holographic diffraction grating where the wavelength components are separated and reflected for independent measurement by the detector(s) (Analytical Spectral Devices Representatives, 2002). Inside the ASD, the fiber optic bundles are separated into three bundles; VNIR (350-1050nm), SWIR1 (900-1850nm), and SWIR2 (1700-2500nm). The overlap in the wavelengths is accounted for when conducting the parabolic corrections to the raw data. ASD data were collected at every location identified throughout the experiment. In order to reduce the effects of noise and the varying light fields experienced in the field, a minimum of sixty spectra samples were taken at each location while simultaneous white plaque spectra was taken under the same illumination geometry. A picture of Dr. Bachmann using an ASD to sample lava rock on the island of Pagan can be seen in Figure 11.

Figure 11.   Dr. Bachmann sampling lava rock

IV.   EXPERIMENT BACKGROUND

A.   OVERVIEW

The Commonwealth of the Northern Mariana Islands 2010 Remote Sensing and Field Calibration Campaign was a multi-agency experiment focused on the collection of airborne HSI with concurrent littoral ground and water validation data at Pagan, Tinian, and Guam, three islands that are included in the Mariana archipelago (Bachmann, et al., 2010). This experiment was one of several since 2007 and was led by the Naval Research Laboratory (NRL) involving the analysis of hyperspectral imagery with littoral ground and water validations. Sponsoring organizations included the Office of Naval Research (ONR) and Marine Corps Forces Pacific (MARFORPAC) and was supported by the NRL, Air Force Research Laboratory (AFRL), the NPS, National Oceanic and Atmospheric Administration (NOAA), MCI MidPac Planning Group, Marine Information Resources Corporation (MIRC), Headquarters Marine Corps (HQMC), Air Flight Services, HyVista Corporation, and Cabras Marine Corporation.

B.   PURPOSE AND SCOPE

The primary focus of the CNMI'10 experiment was to develop trafficability maps, shallow water bathymetry, and target identification using HSI of littoral regions on Pagan, Tinian, and Guam (Bachmann, et al., 2010). The United States Marine Corps is interested about the trafficability of the littoral regions as depicted within the *Marine Corps Warfighting Publication (MCWP) 2-12.1 Geographic Intelligence*. Identified within MCWP 2-12.1 is the creation of a Topographic Platoon-Intelligence Battalion, which provides each Marine Expeditionary Force (MEF) an organic, geographical intelligence (GEOINT) analysis, production, and dissemination capability for tailored geographic views and other GEOINT activities in general support of MEFs or supported commands' intelligence requirements (IRs). Responsibilities include the preparation of coastal hydrographic surveys from the six-fathom depth to extend beyond the beach to the first line of communications and to collect coastal data regarding trafficablility, routes of egress, and inland water bodies (Department of the Navy, 2000). The topographic

platoon then operates a topographic set (TOPOSET) that is a multiworkstation, high-end, geographic information system (GIS) integrating and analyzing multispectral, hyperspectral, and national imagery with GEOINT and other intelligence. Ultimately, military commanders gain the GEOINT, focusing on IPB, from the airborne HSI prior to conducting amphibious operations. The commanders' staff is then better able to exploit both the advantages and disadvantages of the terrain, coasts and waterways, and climatic conditions.

C.   EXPERIMENT DESCRIPTION

The CNMI'10 experiment was divided into three phases:

Phase I   Pagan Campaign

Phase II   Tinian Campaign

Phase III   Guam Campaign

Phase I began on 24 February 2010 in which ten science team members rendezvoused in Saipan to board the motor vessel Micronesian, a 110 foot long charter vessel owned and operated by the Cabras Marine Corporation. The vessel had a crew of about ten personnel to support the team and aid in the on-load and off-load of several Pelican cases of scientific gear. At noon on the 24th, the Micronesian departed Saipan in route to the island of Pagan; approximately 150 miles north of Saipan, see Figure 12.
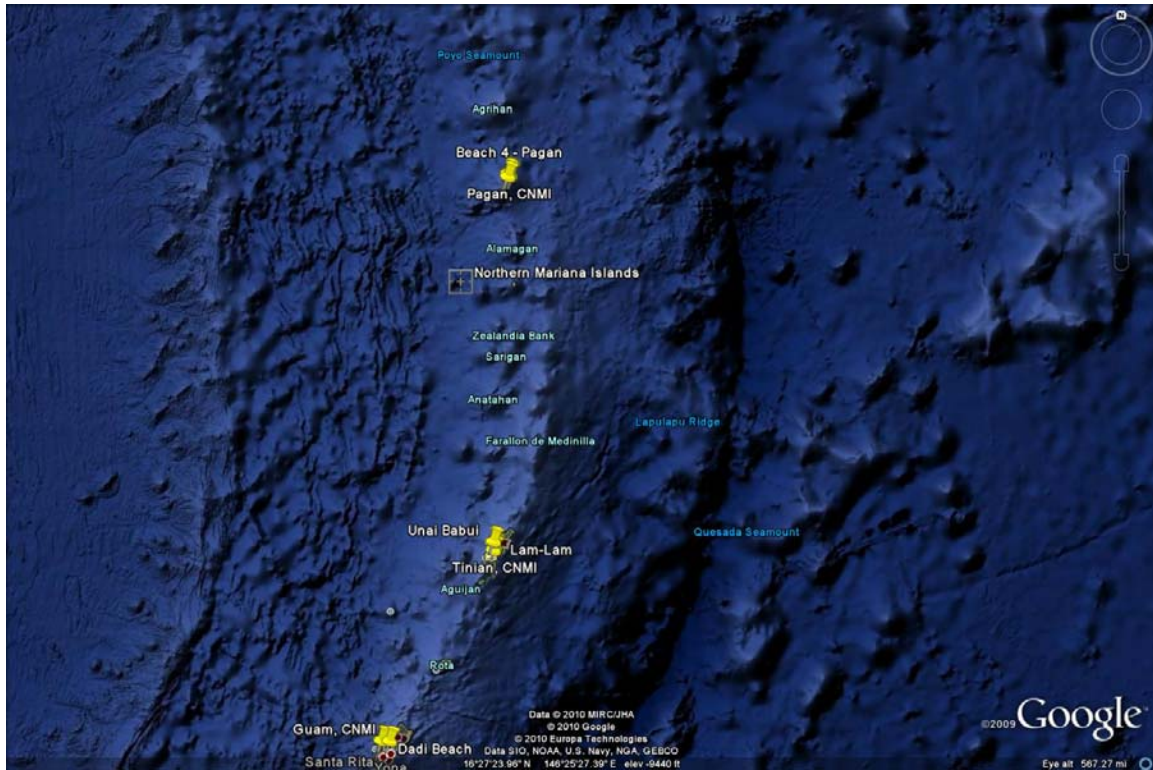
Figure 12.   Mariana Island Chain

After a long evening riding 12–15 foot seas, the ship arrived early the next morning on the western side of Pagan and began making preparations to embark on the island.

Upon completion of the off-load of the science gear, a base global positioning system (GPS) station was positioned at a fixed, elevated position. This base station was used as a positioning reference for the mobile GPS devices throughout the Pagan phase and allows for accurate terrain maps to be built. Four beaches were identified for data collection, three on the west side and one on the east. Only the three western beaches were able to be accessed as the sea state on the east side of the island did not allow for beach access for the team, see Figure 13.
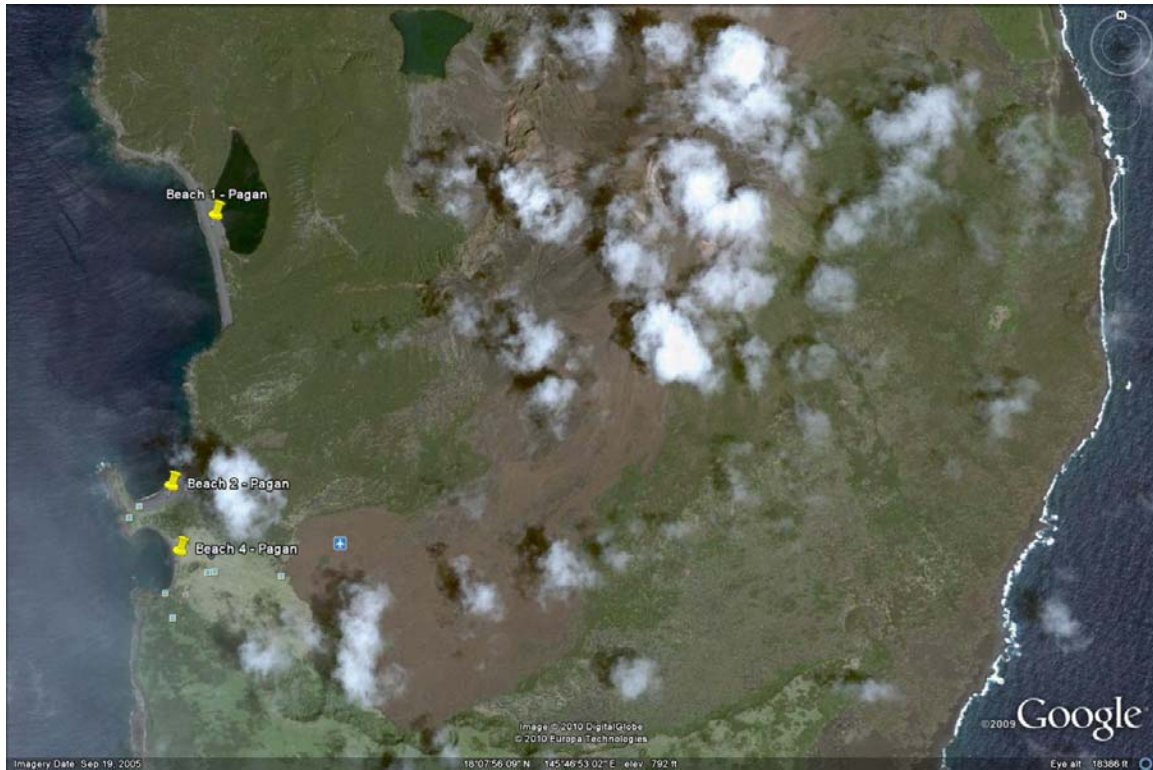
Figure 13.   Pagan Western Sites

Next, several transect locations were first cleared for the absence of unexploded ordinance using a magnetometer and then marked with a flag. The reason for the extra measure of safety requires a brief explanation. During World War II, Pagan was used as a Japanese base during their occupation of the Mariana Islands. When the U.S. liberated the Mariana's, they bombed the Japanese base destroying the airfield, several bunkers, and numerous aircrafts.

Figure 14.   500 lb Bomb

The relics are still present at the island and at least one 500 lb bomb was located by the crew of the Micronesian and pointed out to the science team, see Figure 14. As a precaution, every location identified for scientific purposes was first screened for the absence of any ordinance.

Data collection points on Pagan were:

Three separate beaches involving over 130 data points

Japanese Zero relics

Japanese Bomber relics

World War II Air Raid Bunkers

Various local foliage

Shallow-water bathymetry

Volcanic lava

Black and white calibration panels

Each of the above data points had its reflectance measured with at least sixty samples using an Analytical Spectral Devices Incorporated Full Range FieldSpec Pro spectroradiometer, see Figure 15.

Figure 15.   Dr. Chip Bachmann with Spectroradiometer

The beach data points were measured for their strength using a DCP and a LWD, both described earlier, and then two soil samples were obtained, one for the science team and one for the University of Guam. The University of Guam loaned the team a CIMEL sun-tracking sun photometer, see Figure 16, to obtain accurate aerosol parameters and in turn, received a soil sample from every position the science team observed. The aerosol data is necessary when making atmospheric correction in the hyperspectral imagery.

Figure 16.   Sun Photometer

A GPS measurement was acquired at each data sample location. Additionally, every beach front, in its entirety, was mapped using a kinematic GPS device. Once all of the data is processed, an extremely accurate map can be rebuilt detailing the layout of the terrain and the exact locations of every data point can be identified and compared to the overhead images for further analysis.

The Pagan Phase I ended on the morning of March 3, and the crew headed back to Saipan to begin Phase II on March 4 on the island of Tinian, see Figure 17. Phase II involved data collection on three beach fronts, local foliage samples, and shallow-water bathymetry measurements. The same data collection procedures were followed as in Pagan.
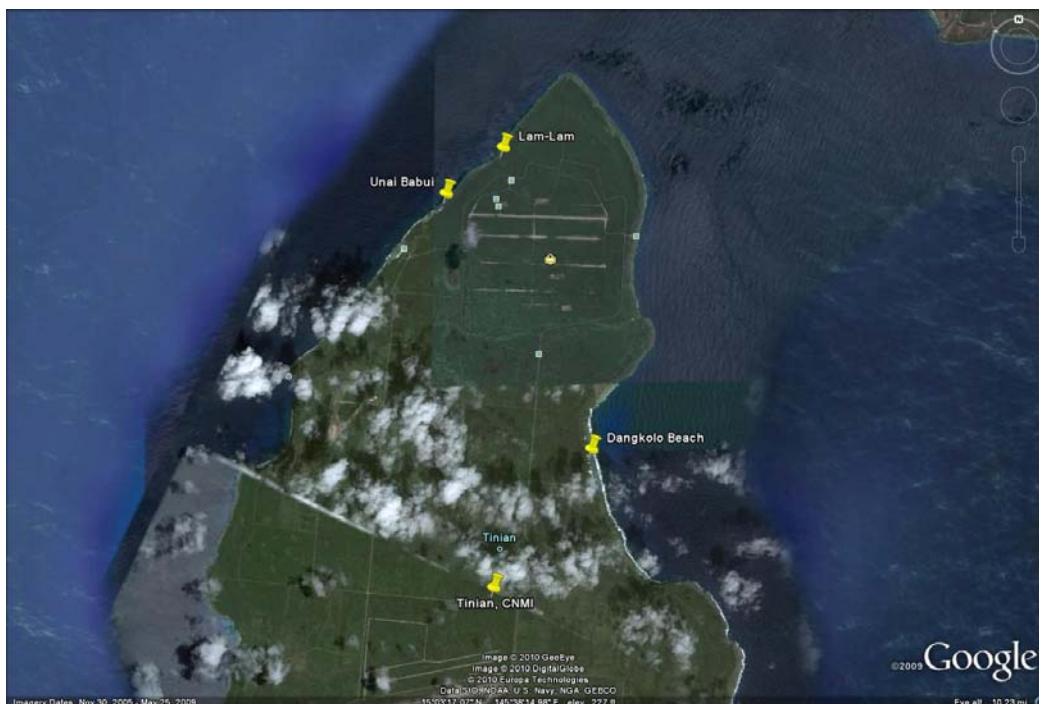
Figure 17.   Tinian

The base GPS station was located at the World War II Tinian airfield, runway Bravo, which is parallel to the runway used during the war to load and launch the atomic bombs, runway Able. Every morning the station was powered on to receive a solid reference point for use when mapping the island. Additionally, GPS tie points were used at three known land survey markers and at corners of large square or rectangular shaped buildings. This allows for corrections to be made to any overhead images as they can be referenced to known locations.

Phase II ended on March 8 and the team flew down to Guam to begin Phase III, which occurred near Apra Harbor on Naval Base Guam, see Figure 18. Phase III also involved the data collection of two beach fronts, local foliage samples, and shallow-water bathymetry and the same procedures as described above were followed.
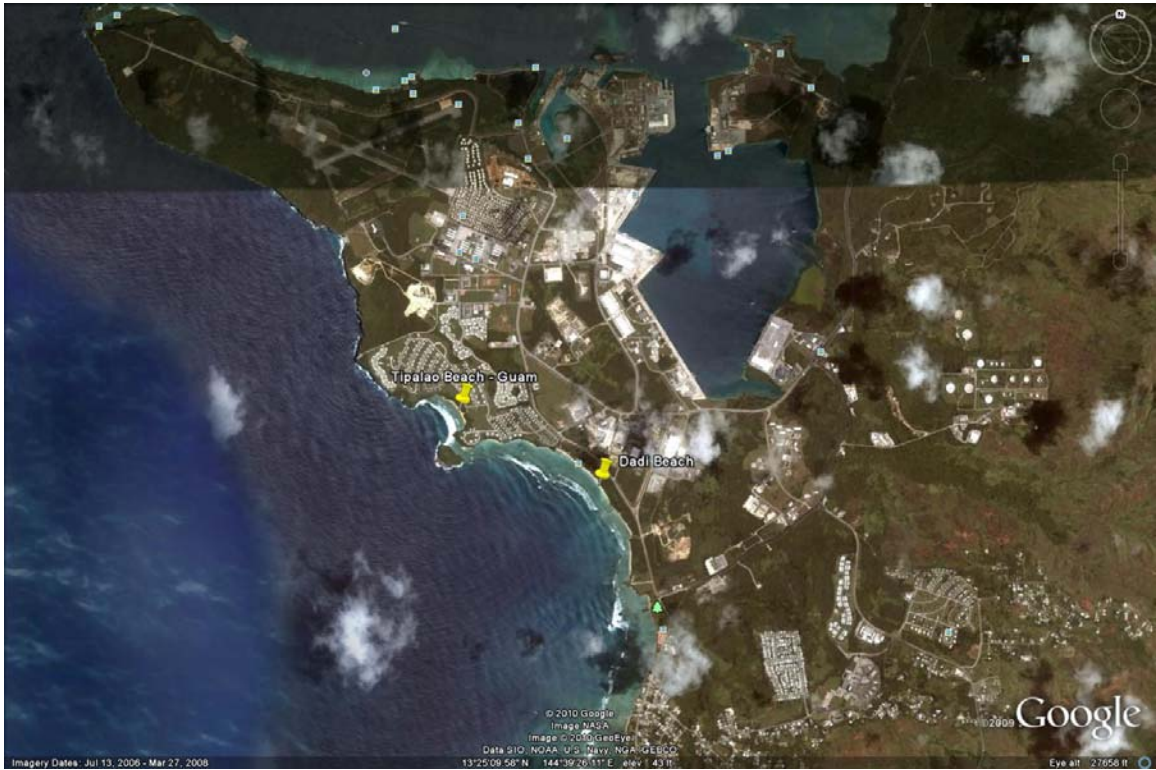
28

Figure 18.   Naval Base Guam

THIS PAGE INTENTIONALLY LEFT BLANK

V.   OBSERVATIONS

A.   GROUND TRUTH DATA ANALYSIS

In situ, data was collected at nearly 130 locations during the CNMI'10 experiment. The coastal regions at Pagan varied significantly from those of Guam and Tinian, while Guam and Tinian were fairly similar to each other. Therefore, this thesis will compare ground truth data from a few locations from Pagan against a few from Tinian. Pagan data points are from the center of Beach 2, conveniently named during the experiment, located on the western side of the island see Figure 19. Tinian data points are from Dangkulo Beach located on the eastern side of the island, see Figure 20.
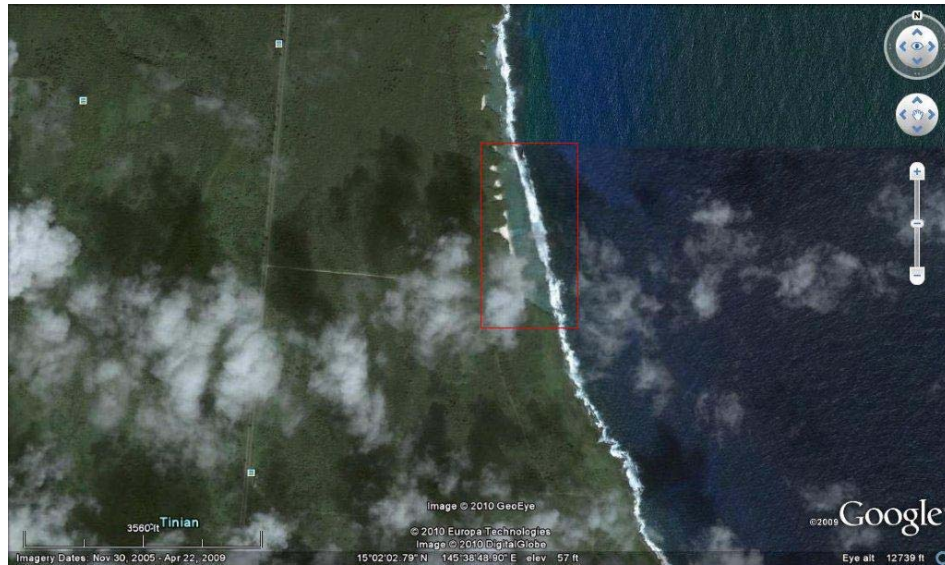

Figure 19.   Pagan Data Locations

Figure 20.   Tinian Data Locations

1.   Lightweight Deflectometer Data

As discussed in Chapter III, the LWD is a device that evaluates the dynamic deflection modulus, known as Evd in MN/m^2, by dropping a known weight from a known height and measuring the pulse generated into the substrate. This modulus is an index of the bearing capacity on subgrade, subsoil, granular layers made of unbound aggregates or recycled materials, backfilling materials, soil stabilization with lime and earth-roads (Zorn, 2005). The LWD data is assigned a trafficability condition using Table 4.

Trafficability	Evd Value (MN/m^2)
Excellent	>28.3
Good	21.6 - 28.2
Fair	14.9 - 21.5
Poor	8.2 - 14.8
Bad	0 - 8.1

Table 4.   Trafficability Conditions

For this thesis, data collected from the LWD from Pagan is isolated to two transects, roughly twenty yards apart, each consisting of a few data points separated by approximately ten yards from beach front to beach head between each point. Three test

32

drops were conducted at each location and the LWD's portable processing and storage system automatically calculates the mean and Evd on site. The Pagan data can be seen in Table 5.

Location ID	Date-2010	Time (Local)	Drop 1 (mm)	Drop 2 (mm)	Drop 3 (mm)	Mean (mm)	Evd (MN/m^2)	Trafficability
PAB2T5-1	1-Mar	10:12	2.936	2.794	2.361	2.697	8.3	Poor
PAB2T5-2	1-Mar	10:32	8.676	4.952	4.188	5.939	3.8	Bad
PAB2T5-3	1-Mar	10:37	5.358	4.142	3.914	4.471	5.0	Bad
PAB2T5-4	1-Mar	11:00	11.601	5.052	4.366	7.006	3.2	Bad
PAB2T5-5 # 1	1-Mar	11:06	10.764	3.630	3.493	5.962	3.8	Bad
PAB2T5-5 # 2	1-Mar	11:10	12.138	4.585	4.730	7.151	3.1	Bad
PAB2T6-1	1-Mar	10:17	5.841	2.793	2.427	3.687	6.1	Bad
PAB2T6-2	1-Mar	10:25	5.449	4.489	4.080	4.673	4.8	Bad
PAB2T6-3	1-Mar	10:45	12.249	5.146	4.049	7.148	3.1	Bad
PAB2T6-4	1-Mar	10:51	6.254	4.767	5.771	5.597	4.0	Bad
PAB2T6-5	1-Mar	11:15	10.361	4.634	3.892	6.296	3.6	Bad

Table 5.   Pagan LWD Data

The data from Tinian were from the beach named Dangkulo and the results can be seen in Table 6.

Location ID	Date-2010	Time (Local)	Drop 1 (mm)	Drop 2 (mm)	Drop 3 (mm)	Mean (mm)	Evd (MN/m^2)	Trafficability
TNUDT1-1	6-Mar	13:49	0.826	0.537	0.397	0.587	38.3	Excellent
TNUDT1-2	6-Mar	14:07	6.129	2.803	1.994	3.642	6.2	Bad
TNUDT1-3	6-Mar	15:25	6.246	2.173	8.051	5.490	4.1	Bad
TNUDT1-4	6-Mar	14:52	5.244	3.927	2.043	3.738	6.0	Bad
TNUDT1-5	6-Mar	15:13	6.120	2.505	3.534	4.053	5.6	Bad
TNUDT1-6	6-Mar	15:43	3.703	1.208	1.039	1.983	11.3	Poor
TNUDT2-1	6-Mar	16:14	1.675	0.683	0.558	0.972	23.1	Good
TNUDT2-2, #1	6-Mar	16:21	10.069	41.880	2.639	18.196	1.2	Bad
TNUDT2-2, #2	6-Mar	16:23	8.483	3.195	2.118	4.599	4.9	Bad
TNUDT2-3	6-Mar	16:34	6.322	2.890	2.307	3.840	5.9	Bad
TNUDT2-4	6-Mar	16:44	6.912	2.563	2.184	3.886	5.8	Bad
TNUDT2-5	6-Mar	16:54	5.845	2.773	2.052	3.557	6.3	Bad
TNUDT3-1	7-Mar	9:41	3.338	3.228	2.751	3.106	7.2	Bad
TNUDT3-2	7-Mar	9:45	5.283	3.569	2.896	3.916	5.7	Bad
TNUDT3-3	7-Mar	9:52	6.432	3.294	1.760	3.829	5.9	Bad
TNUDT3-4	7-Mar	10:04	4.295	2.404	1.678	2.792	8.1	Bad
TNUDT3-5	7-Mar	10:15	9.465	1.615	1.875	4.318	5.2	Bad
TNUDT3-6	7-Mar	10:22	4.577	3.077	2.441	3.365	6.7	Bad

Table 6.   Tinian LWD Data

Analysis of the data clearly indicates how the data points closer to the water's edge have a higher Evd than the other data points. This is also indicated by the increased deflection value as the data points moved away from the water. One can also see that the average Evd from the data collected on Tinian indicates that the beach front is stronger than Pagan beachfront. However, to put these numbers in perspective, a table of various materials is listed in Table 7. Pascal to Newton per square meter conversion has a multiple of one. It should be noted that several of the data points sampled in the CNMI'10 campaign failed to surpass the elastic modulus value of rubber.

Material	Elastic Modulus	
	MPa	psi
Diamond	1,200,000	170,000,000
Steel	200,000	30,000,000
Aluminum	70,000	10,000,000
Wood	7,000-14,000	1,000,000-2,000,000
Crushed Stone	150-300	20,000-40,000
Silty Soils	35-150	5,000-20,000
Clay Soils	35-100	5,000-15,000
Rubber	7	1,000

Table 7.   Modulus of Elasticity for Various Materials (From Muench, et al.)

2.   Dynamic Cone Penetrometer Data

A DCP was used during the CNMI'10 campaign to measure in situ soil strength. This was done by dropping a ten pound hammer onto an anvil to drive a 60 degree cone into the soil. Each strike of the hammer was recorded for the amount of penetration into the ground after each drop. The amount of penetration from each drop is known as the DCP penetration index (DPI). This DPI can be correlated to the CBR, which is the measured pressure for site soils versus the pressure to achieve equal penetration on standard soil. Plots were generated illustrating the depth below the surface the rod was driven versus CBR for each data point, see figures below. According to the Minnesota Department of Transportation, any CBR value of at least six is required to minimize rutting damage to the finished grade prior to paving and CBR values less than eight may require remedial procedures, such as subcutting, drying and recompaction, or backfilling with granular borrow or lime treatment (MNDoT).
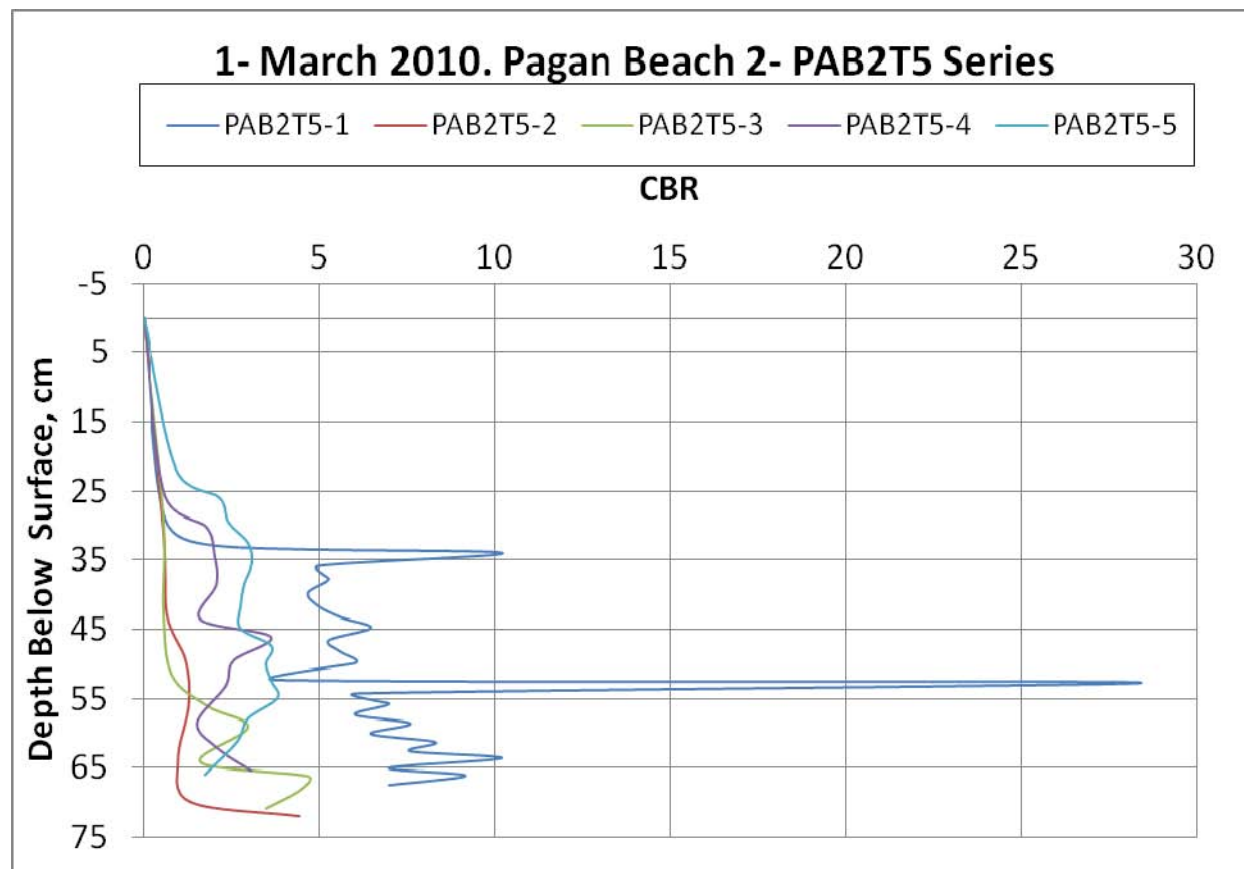
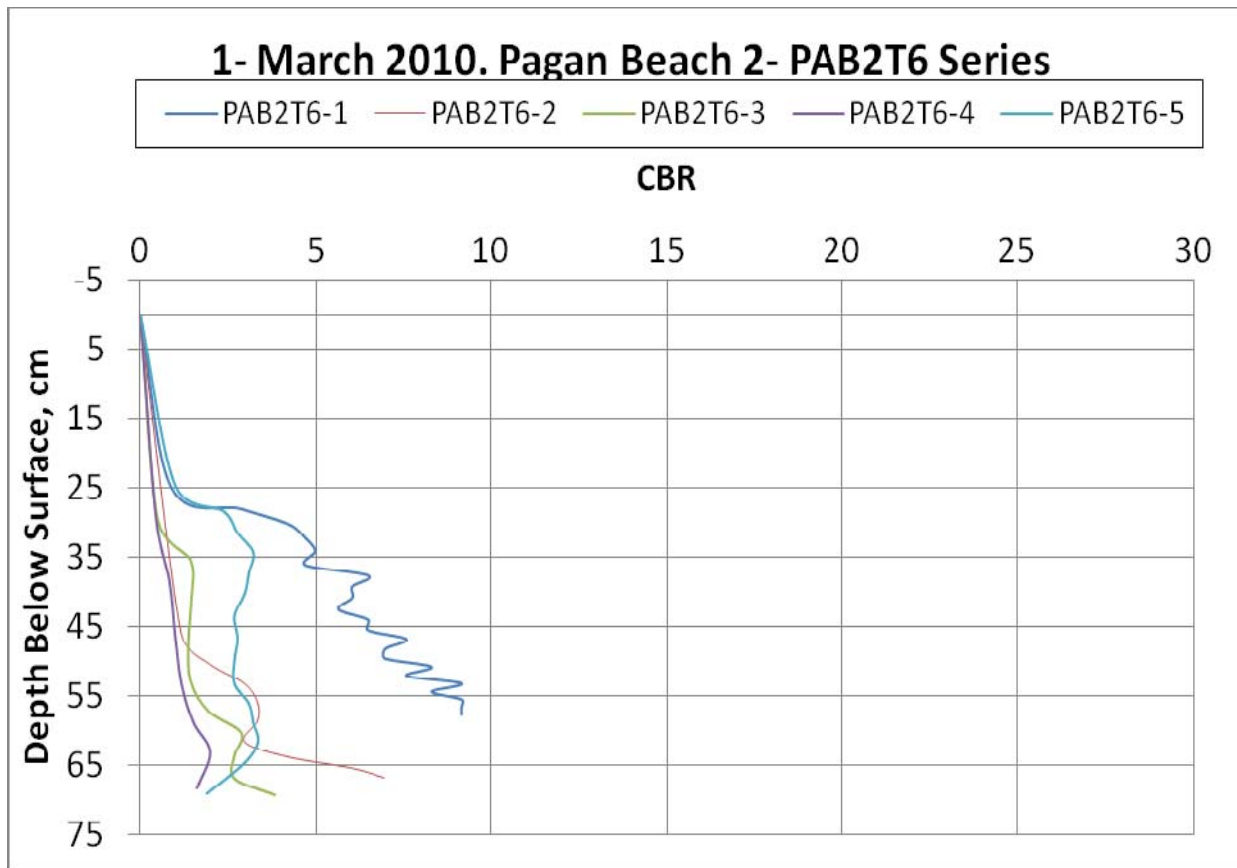Figure 21.　　Pagan Beach 2 Transect 5 CBR Data

Figure 22.   Pagan Beach 2 Transect 6 CBR Data

The Tinian Data for each of the three transects can be seen below.
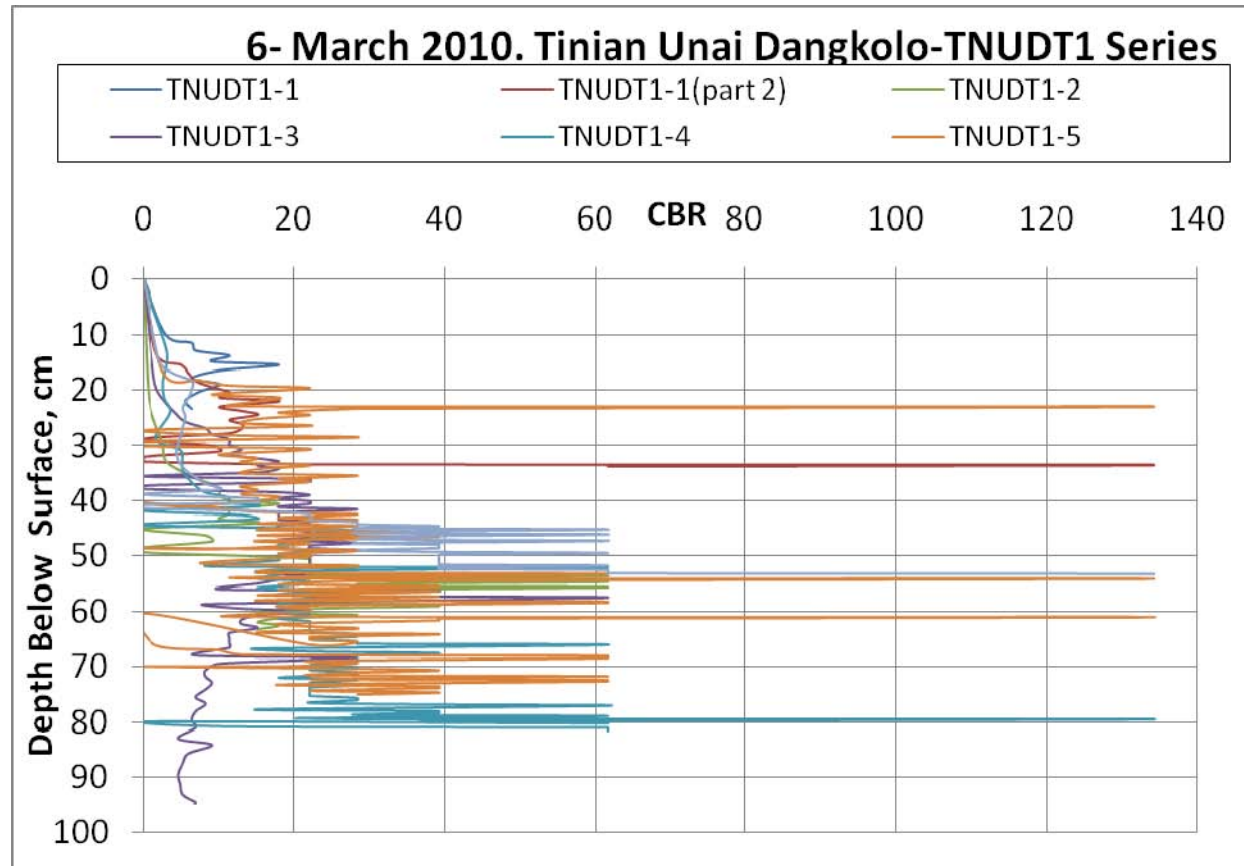

Figure 23.   Dangkulo Transect 1 CBR Data
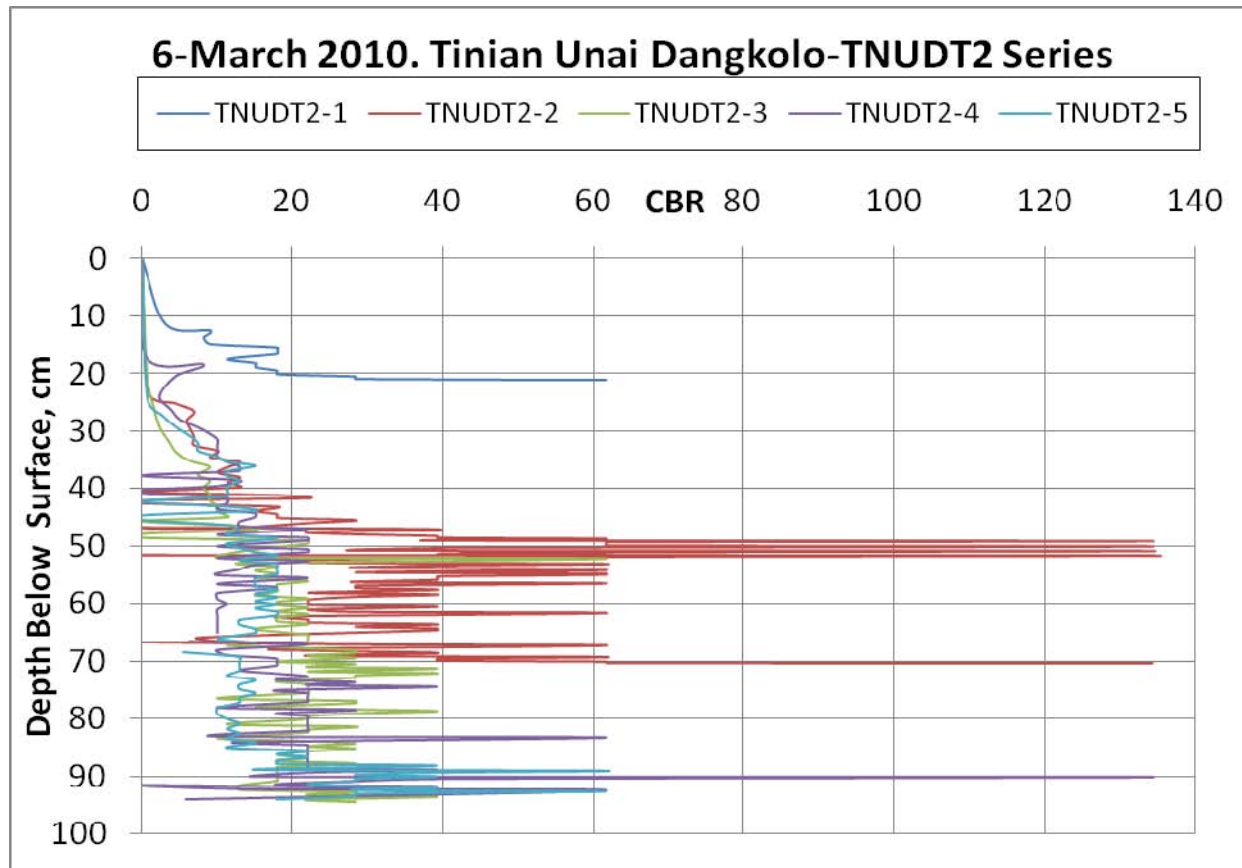
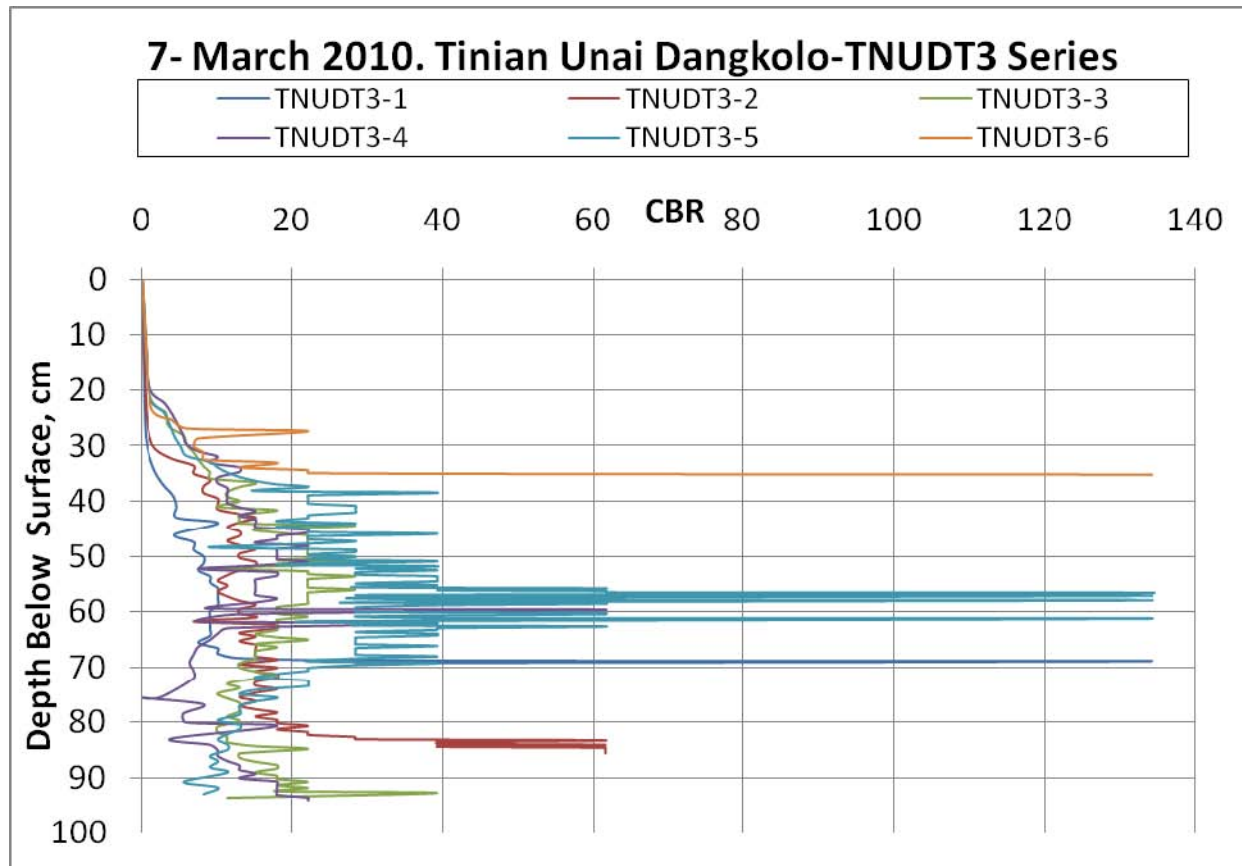Figure 24.   Dangkulo Transect 2 CBR Data

Figure 25.   Dangkulo Transect 1 CBR Data

Visual analysis illustrates that the overall CBR values for Pagan are significantly lower than the data points from Tinian. In fact, many of the data points from Pagan fall close to the threshold on requiring remedial procedures as per the Minnesota Department of Transportation. By plotting the CBR results from the DCP tests, it is clear that Tinian is a stronger beachfront.

3. Grain Size Distribution and Moisture Content

Upon completion of the DCP and LWD tests at each data point, a core sample of approximately three inches was taken and bagged for analysis of grain sizes and moisture content. Once back in the laboratory, the core sample was first weighed to obtain its moisture weight. Next, the sample was heated in a microwave oven to dry out the moisture and then reweighed. The moisture content was then calculated in both weight and percentage. The results from Pagan can be seen in Table 8.

Sample Name	Date (2010)	Wet Weight (g)	Dry Weight (g)	(Wet-Dry) (g)	Soil Moisture Content (w) %
PAB2T5-1	1-Mar	415.00	392.59	22.41	5.71
PAB2T5-2	1-Mar	475.18	458.89	16.29	3.55
PAB2T5-3	1-Mar	497.08	481.01	16.07	3.34
PAB2T5-4	1-Mar	275.18	268.05	7.13	2.66
PAB2T5-5	1-Mar	733.65	709.52	24.13	3.40
PAB2T6-1	1-Mar	462.02	442.58	19.44	4.39
PAB2T6-2	1-Mar	375.72	365.02	10.70	2.93
PAB2T6-3	1-Mar	495.29	478.94	16.35	3.41
PAB2T6-4	1-Mar	361.08	349.46	11.62	3.33
PAB2T6-5	1-Mar	527.94	513.23	14.71	2.87

Table 8.   Pagan Soil Moisture Data

Tinian moisture data can be seen in Table 9.

Sample Name	Date (2010)	Wet Weight (g)	Dry Weight (g)	(Wet-Dry) (g)	Soil Moisture Content (w) %
TNUDT1-1	6-Mar	531.30	416.40	114.90	27.59
TNUDT1-2	6-Mar	381.62	371.67	9.95	2.68
TNUDT1-3	6-Mar	367.55	338.40	29.15	8.61
TNUDT1-4	6-Mar	456.62	434.50	22.12	5.09
TNUDT1-5	6-Mar	407.76	377.09	30.67	8.13
TNUDT1-6	6-Mar	454.22	393.50	60.72	15.43
TNUDT2-1	6-Mar	482.87	357.98	124.89	34.89
TNUDT2-2	6-Mar	536.58	505.55	31.03	6.14
TNUDT2-3	6-Mar	456.53	413.37	43.16	10.44
TNUDT2-4	6-Mar	368.85	332.75	36.10	10.85
TNUDT2-5	6-Mar	388.97	364.34	24.63	6.76
TNUDT3-1	7-Mar	448.05	408.53	39.52	9.67
TNUDT3-2	7-Mar	434.30	387.70	46.60	12.02
TNUDT3-3	7-Mar	573.19	538.53	34.66	6.44
TNUDT3-4	7-Mar	440.51	412.28	28.23	*6.85*
TNUDT3-5	7-Mar	N/A	N/A	N/A	N/A
TNUDT3-6	7-Mar	N/A	N/A	N/A	N/A

Table 9.   Tinian Soil Moisture Data

Upon completion of determining the moisture content of each sample, the soil was placed in a shaker system consisting of sieves ranging in size from 25 microns to 50,000 microns. The sieve shaker ran for ten minutes and anything smaller than 25 microns fell into a pan at the bottom. The grain size distribution was then recorded and plotted. Pagan and Tinian results can be seen in the following figures.
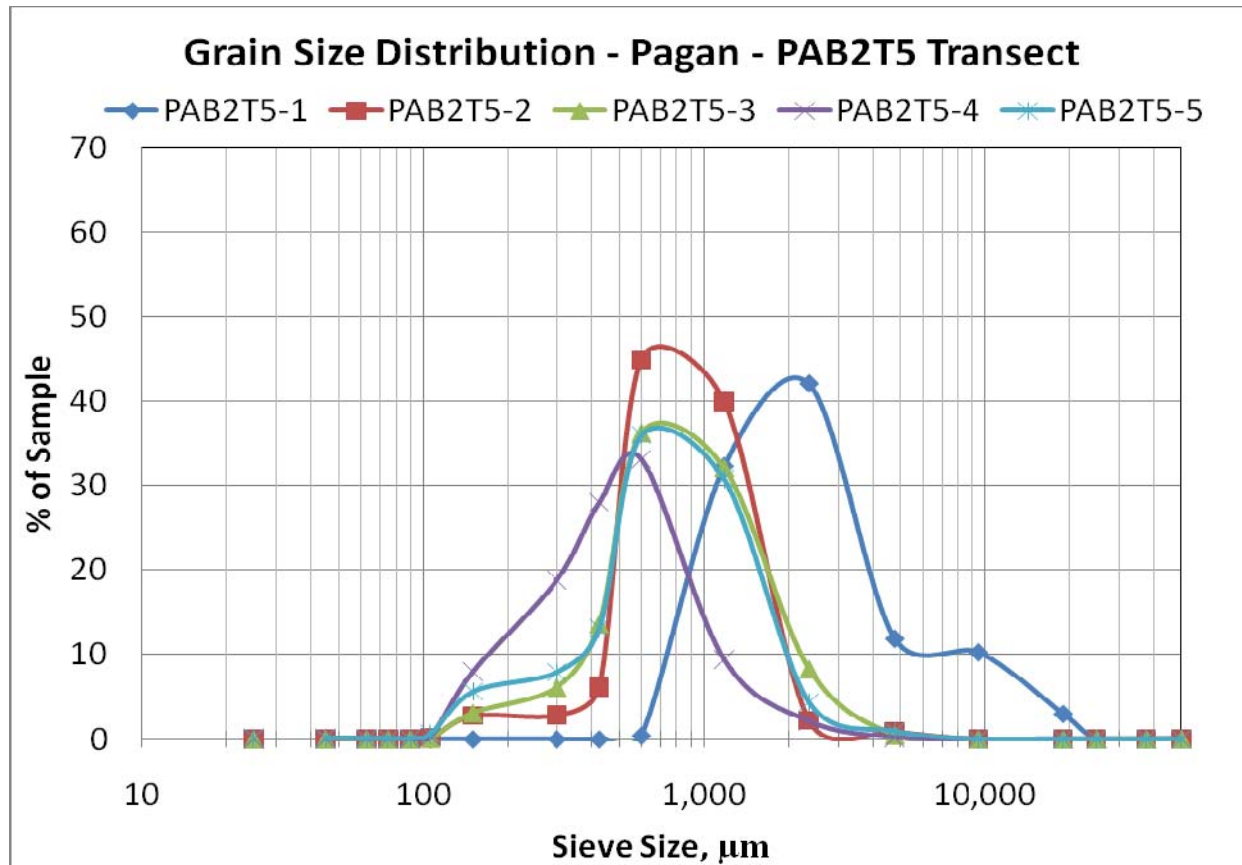
Figure 26.   Pagan Grain Size Distribution Transect 5
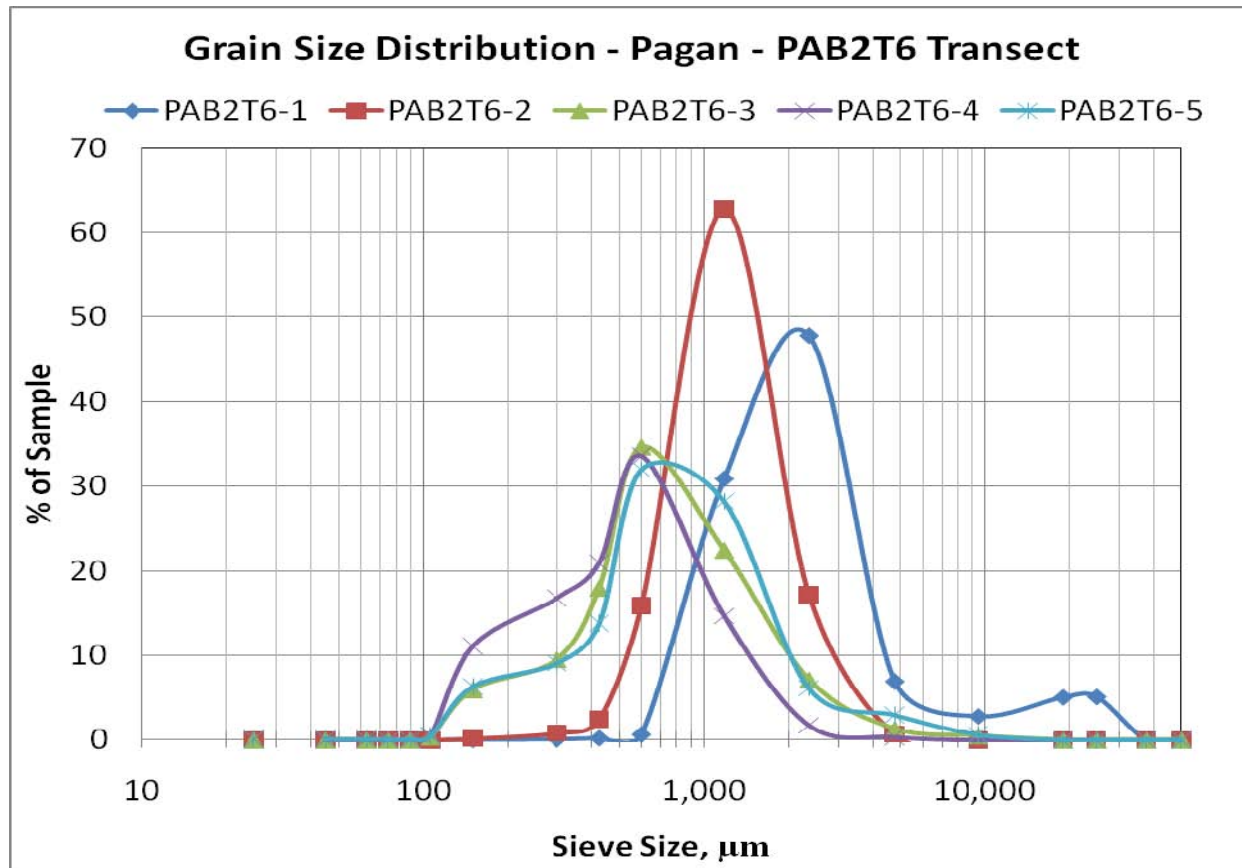
Figure 27.   Pagan Grain Size Distribution Transect 6
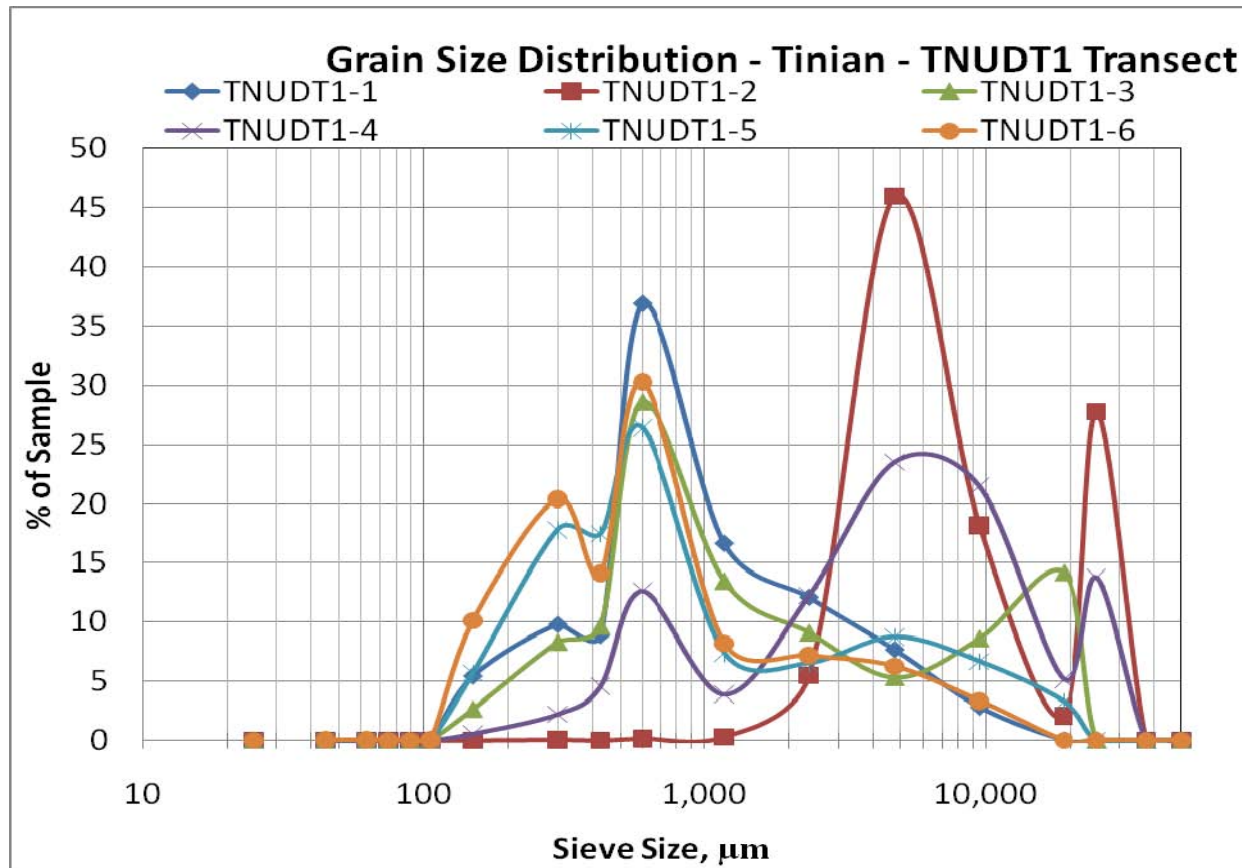
Figure 28.   Tinian Grain Size Distribution Transect 1
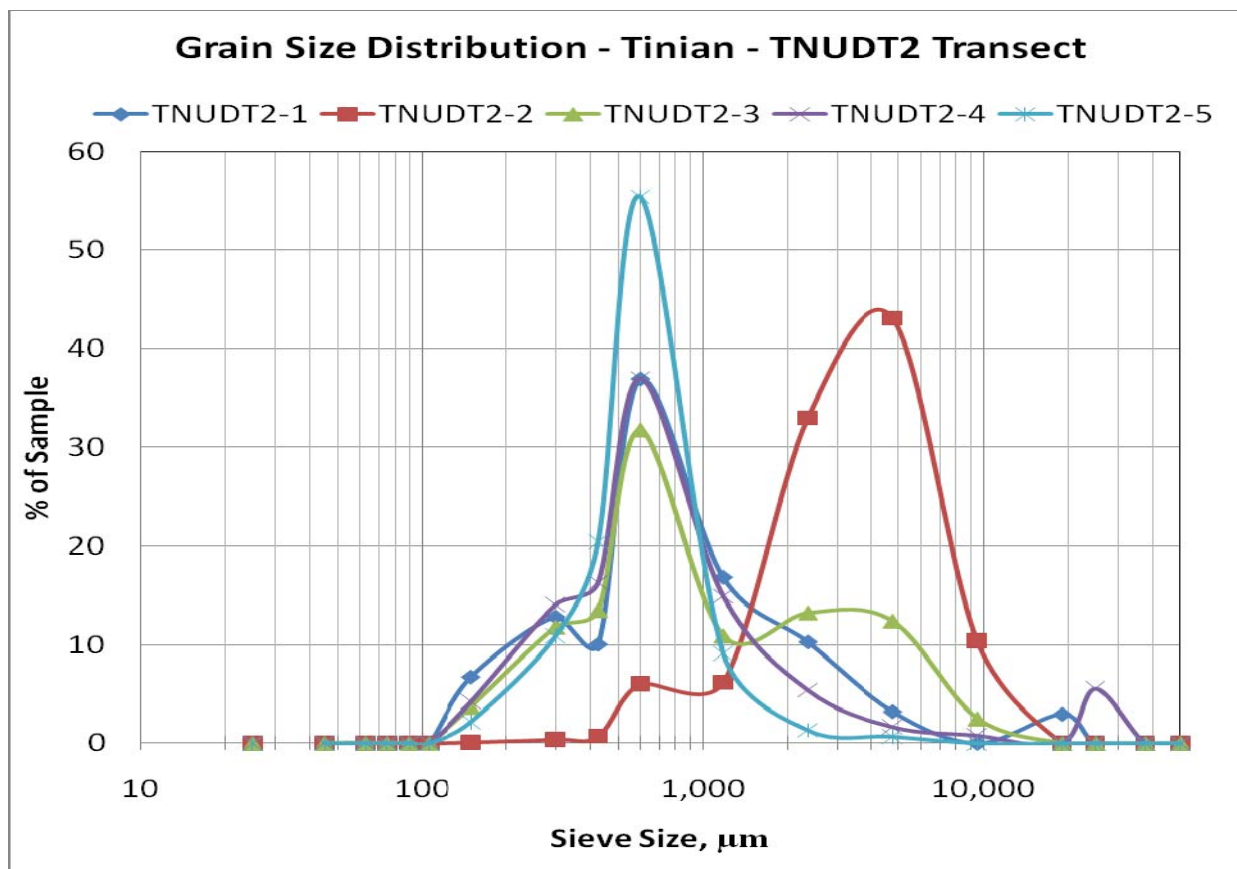
Figure 29.   Tinian Grain Size Distribution Transect 2
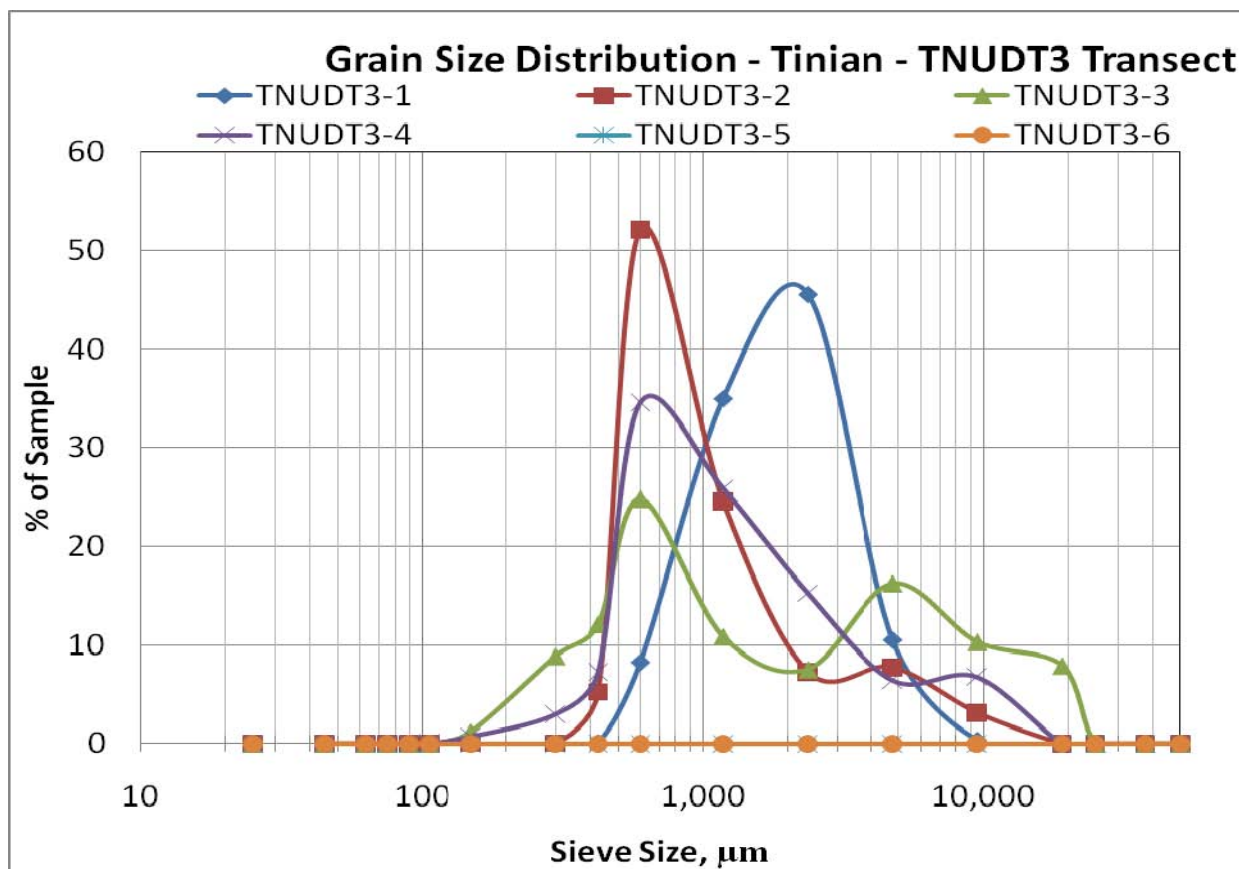
Figure 30.   Tinian Grain Size Distribution Transect 3

Analysis of the grain size distribution indicates how varied the distribution is for Tinian when compared to Pagan. As discussed earlier, the distribution is yet another factor that determines the soil strength. Soils that possess a varied grain size distribution allows for the smaller grain sizes to fall into the voids creating a stronger substrate. The DCP and LWD data confirm this indicating that Tinian has a stronger substrate when compared to Pagan.

B. SPECTRAL ANALYSIS

1. ASD Spectral Analysis

A spectral signature was obtained from each data location along with the physical data using the FieldSpec Pro Spectrometer, referred to as the ASD. The data were collected as a raw digital number, raw DN, and then processed into reflectance using the RS^3 program. Pagan reflectance data, scaled from 0 to 1, can be seen in Figure 31 and Figure 32.

Since sky conditions were not always favorable, it was necessary to cross-calibrate the ASD instruments in order to measure a transfer function. The transfer function is measured by normalizing the two spectrometers by a white-to-white plaque calibration. The transfer function is then used to normalize the data collected. This dual-spectrometer approach was developed by the NRL and is discussed in further detail in an article by Dr. Chip Bachmann and his team titled: *A Practical Dual-Spectrometer Approach to Measuring In Situ Spectral Reflectance Under Adverse Sky Conditions.* However, at the time this thesis was written, the process for normalizing the data caused spurious spikes (false maxima and absorption features) in some of the reflectance calculations and is the cause for the noisy reflectance signatures seen in Figure 32. The data has since been reprocessed by the NRL and an updated graph of transect six can be seen in Figure 33. However, due to time constraints, it was not possible for this updated reflectance to be used for the work in this thesis.
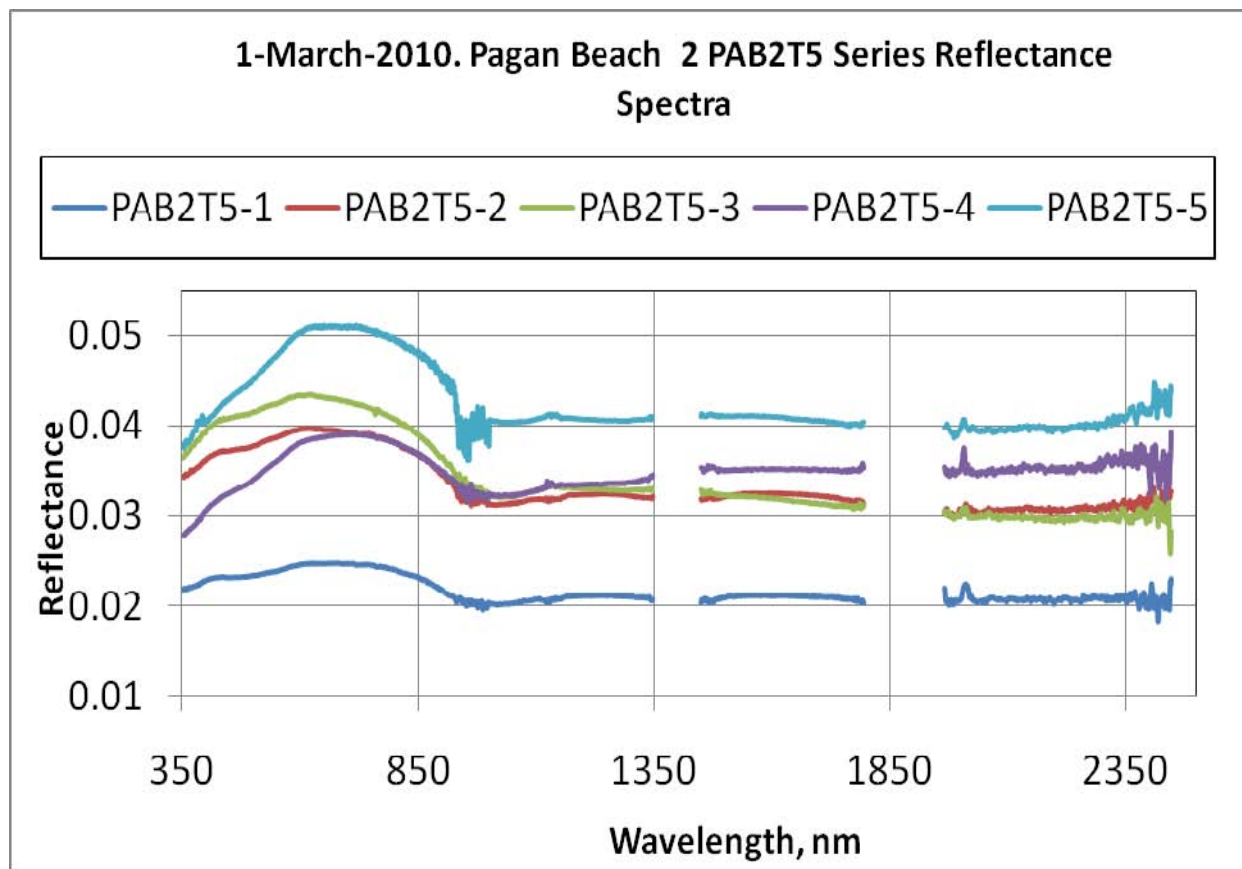
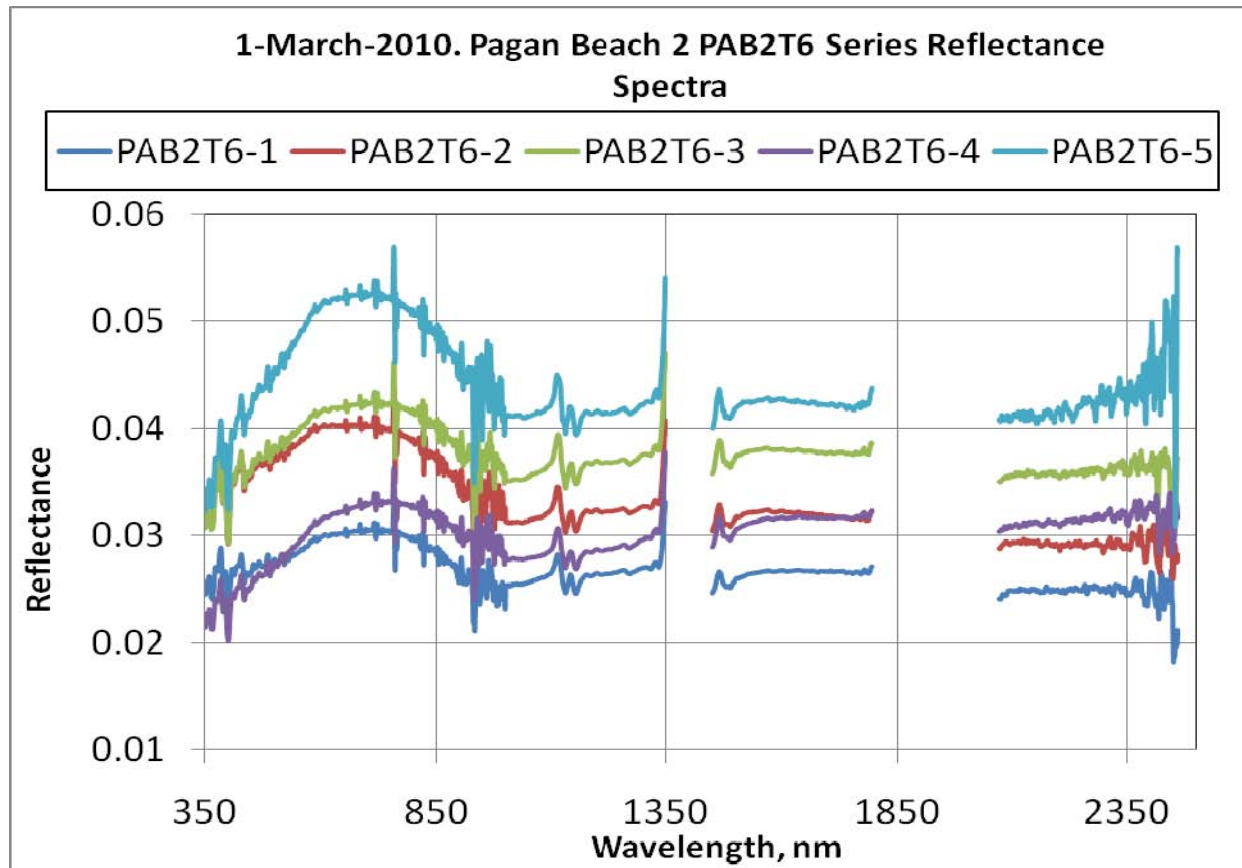Figure 31.   Pagan ASD Reflectance Graph Transect 5

Figure 32.　　　　Pagan ASD Reflectance Graph Transect 6
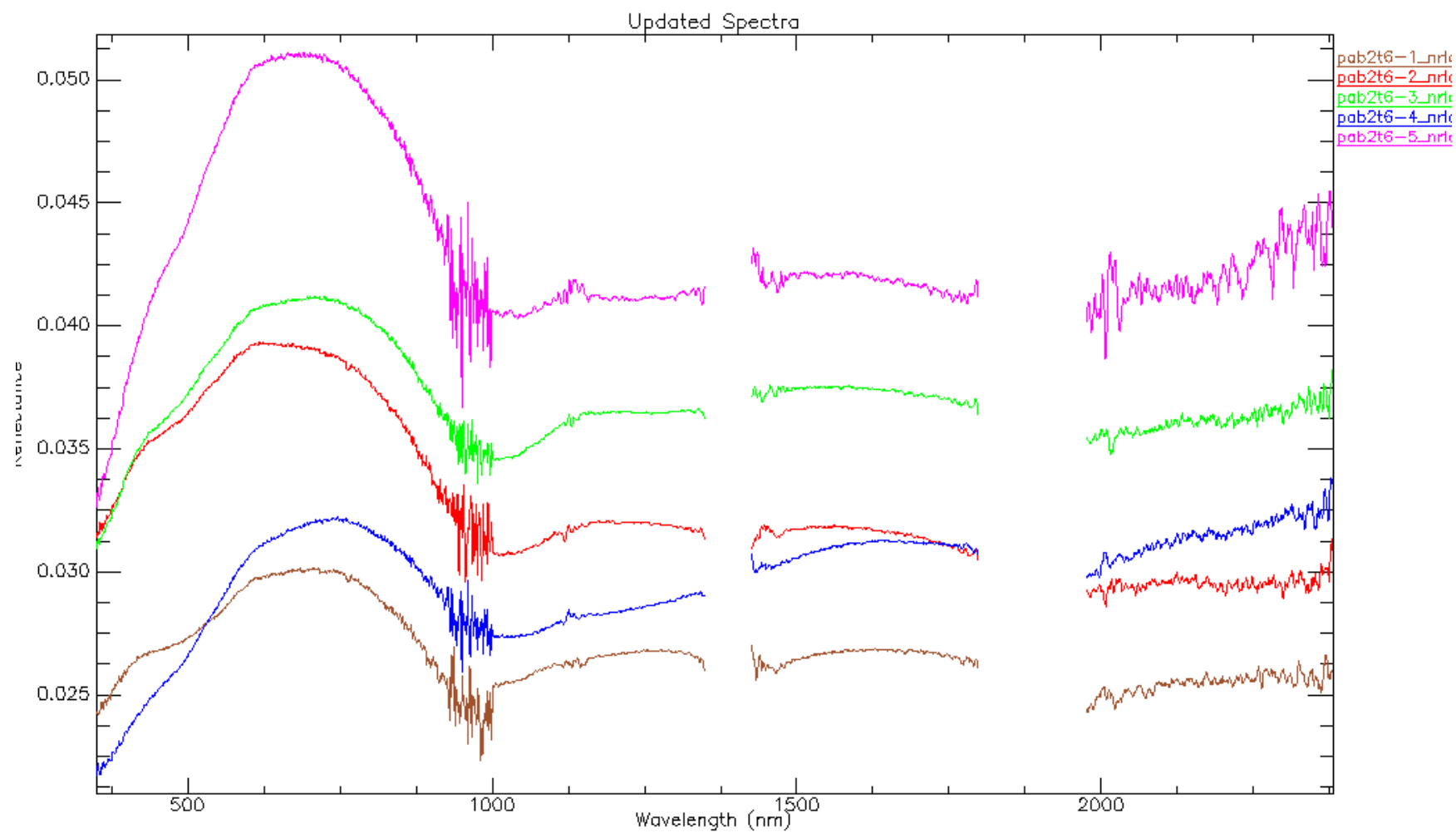
Figure 33.	Updated Pagan ASD Reflectance Graph Transect 6

Tinian reflectance data can be seen in the following three figures.
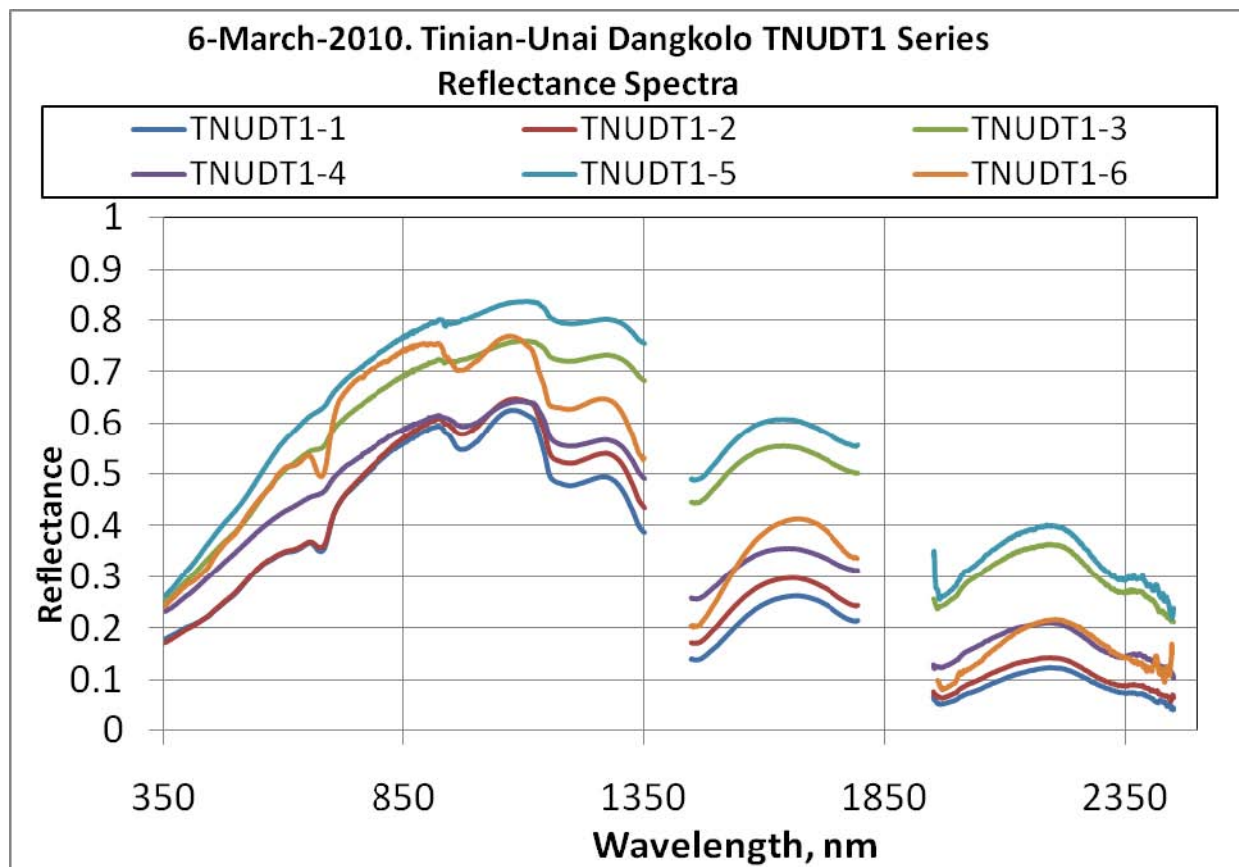

Figure 34.   Tinian ASD Reflectance Graph Transect 1
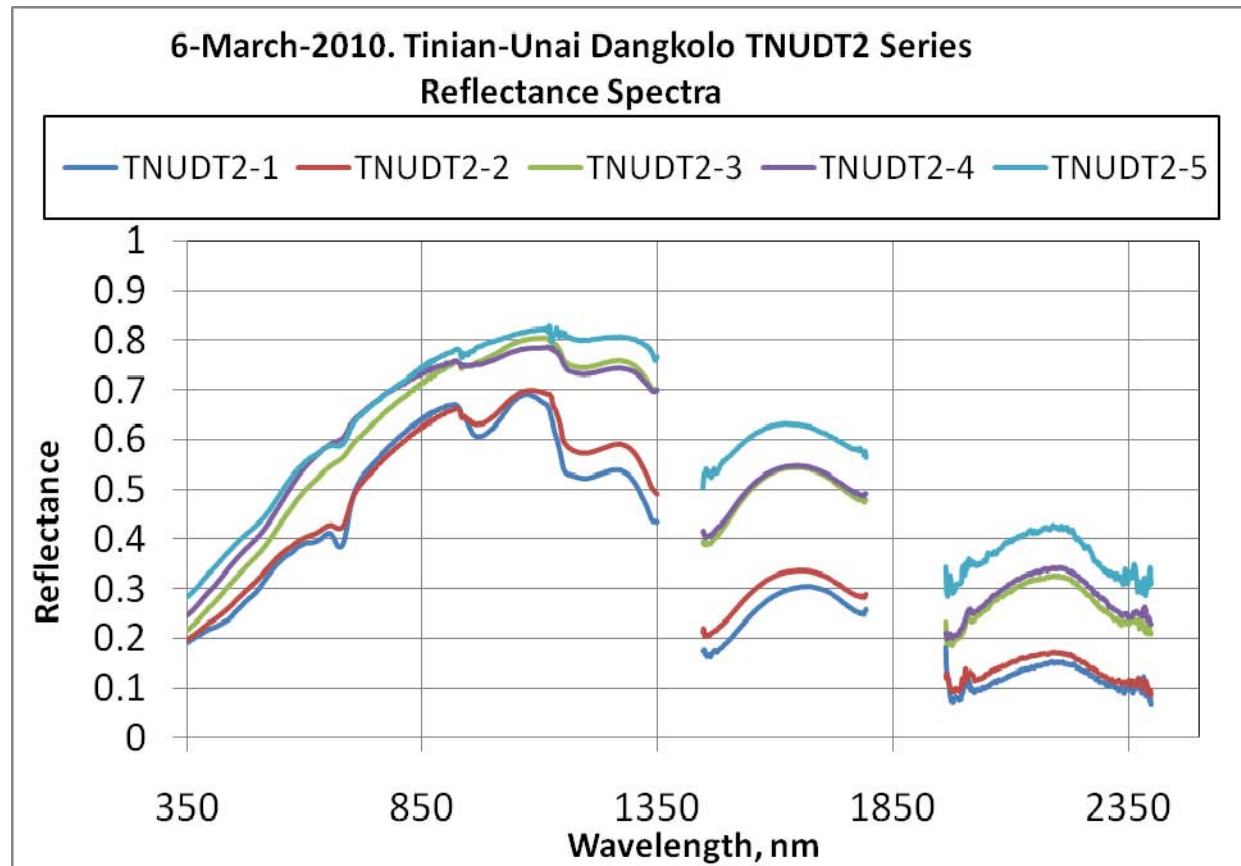
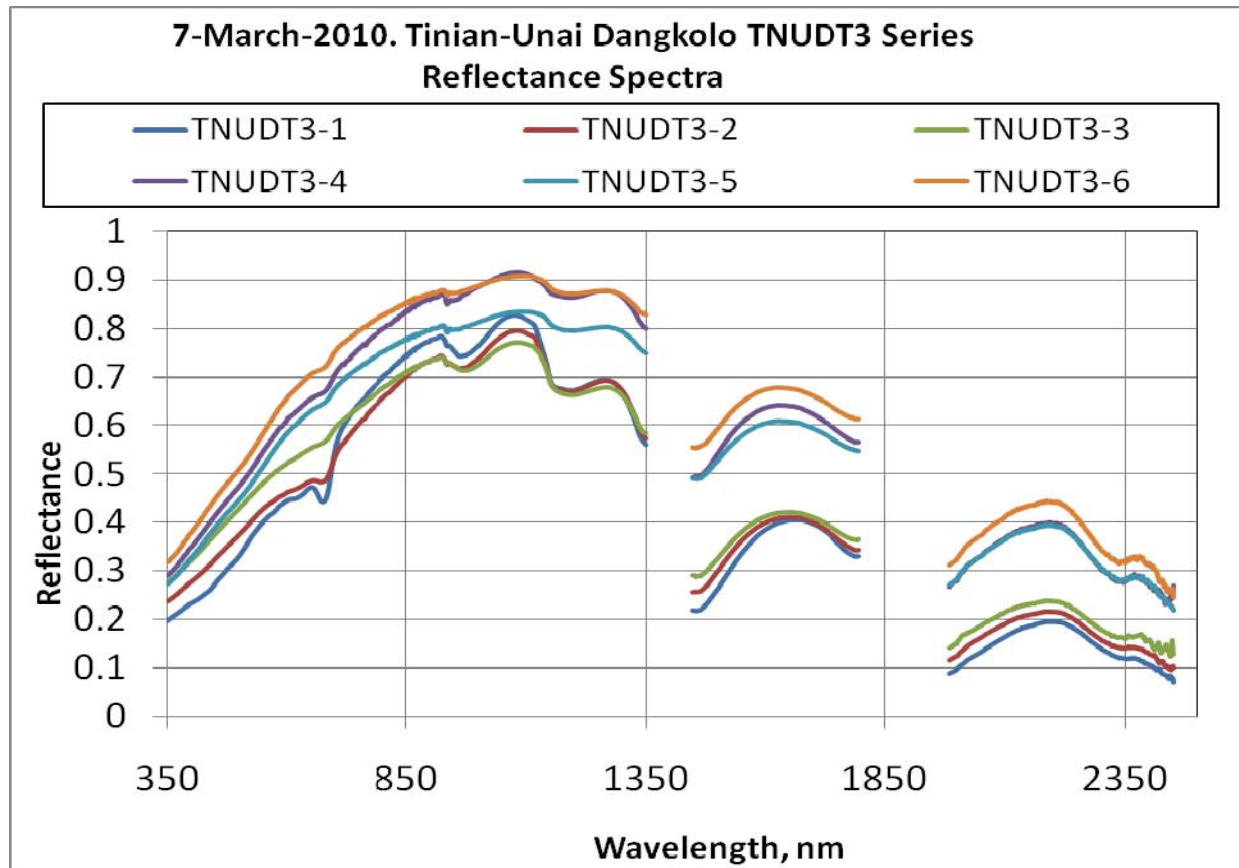Figure 35.   Tinian ASD Reflectance Graph Transect 2

Figure 36.   Tinian ASD Reflectance Graph Transect 3

The breaks in the spectra are caused by atmospheric absorption. Analyzing the graphs above, one can see how the reflectance signature from Tinian is larger than the signatures from Pagan. This can be attributed to the darker volcanic sand that was found on Pagan versus the lighter colored sand found on Tinian.

2.   Airborne Spectral Analysis

HyVista's HYMAP sensor was flown above each island throughout the CNMI'10 campaign gathering several images in both the mornings and afternoons. However, since the largest contributor to errors in HSI is caused by the atmosphere, correction algorithms needed to be applied to the images prior to using the images. The images were processed for atmospheric interferences using a program called The Algorithm Formerly Known as Atmospheric Removal (Tafkaa). Tafkaa was developed by the NRL and takes absorption parameters for H_2O, CO_2, N_2O, CO, CH_4, and O_2 and it then applies those parameters to the hyperspectral image (Montes & Davis, 2004). This method is complex, but previous experiments have shown it provides more accurate corrections than other methods.

Initially, production of the trafficability maps used the spectral library containing the spectra as measured in situ. However, this approach produced extremely poor results. When analyzing the reason for the non-classification of any matching spectra, it was suspected that the HSI spectral signature from the HyMap image did not match closely enough to that of the in situ spectral library. Since the in situ soil strength data was known and each location was identified by its GPS location, the in-scene spectra were used as the reference spectral library to generate the trafficability maps.

To illustrate the spectral variations, graphs of ASD and HyMap spectra for data location PAB2T6-5 can be seen in Figure 37. From this graph, one can see how the reflectance measured in situ slightly differs from what HyMap gathered. While location PAB2T6-5 was one of the closer matches in the spectral comparison, the difference was still enough for ENVI to make either false or non-classification of spectral matches. An example of a poor spectral match can be seen in Figure 38.
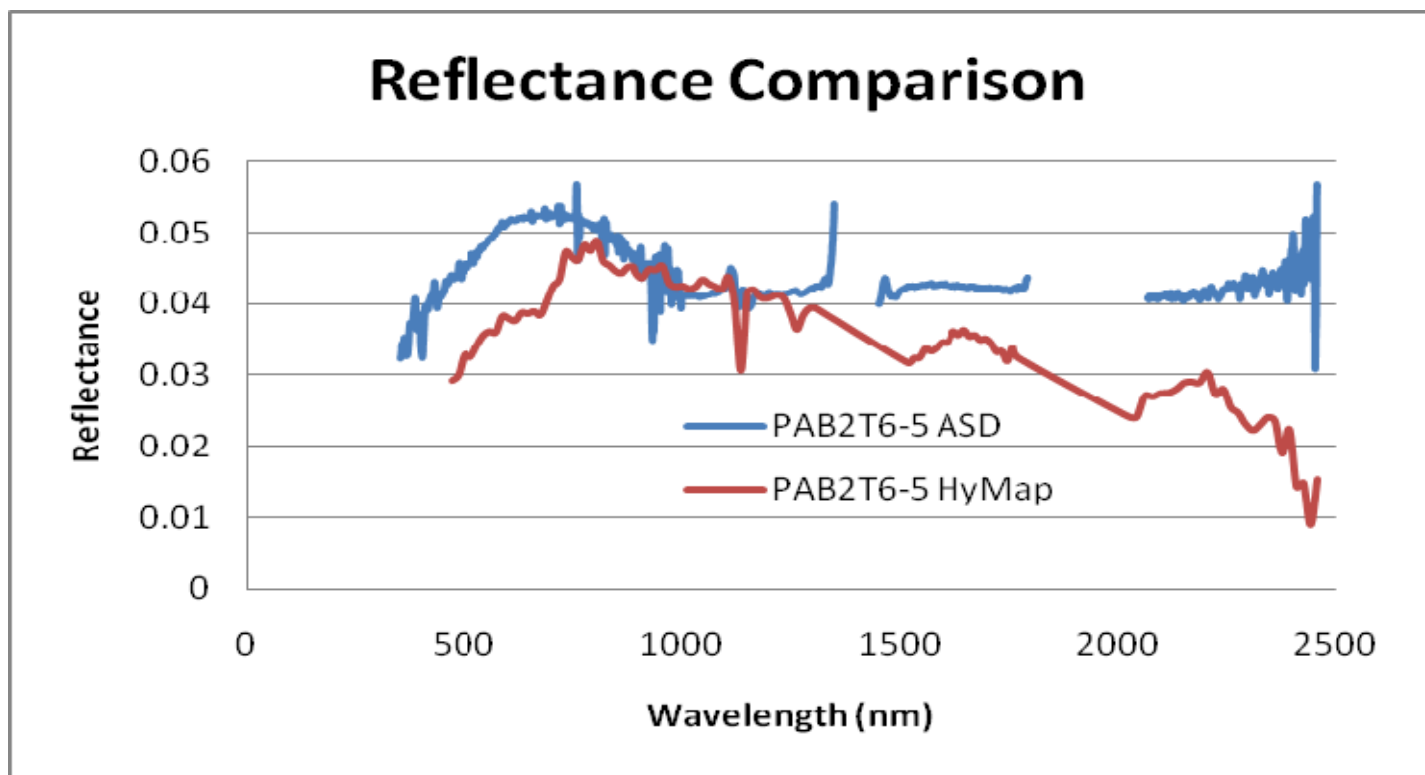
55

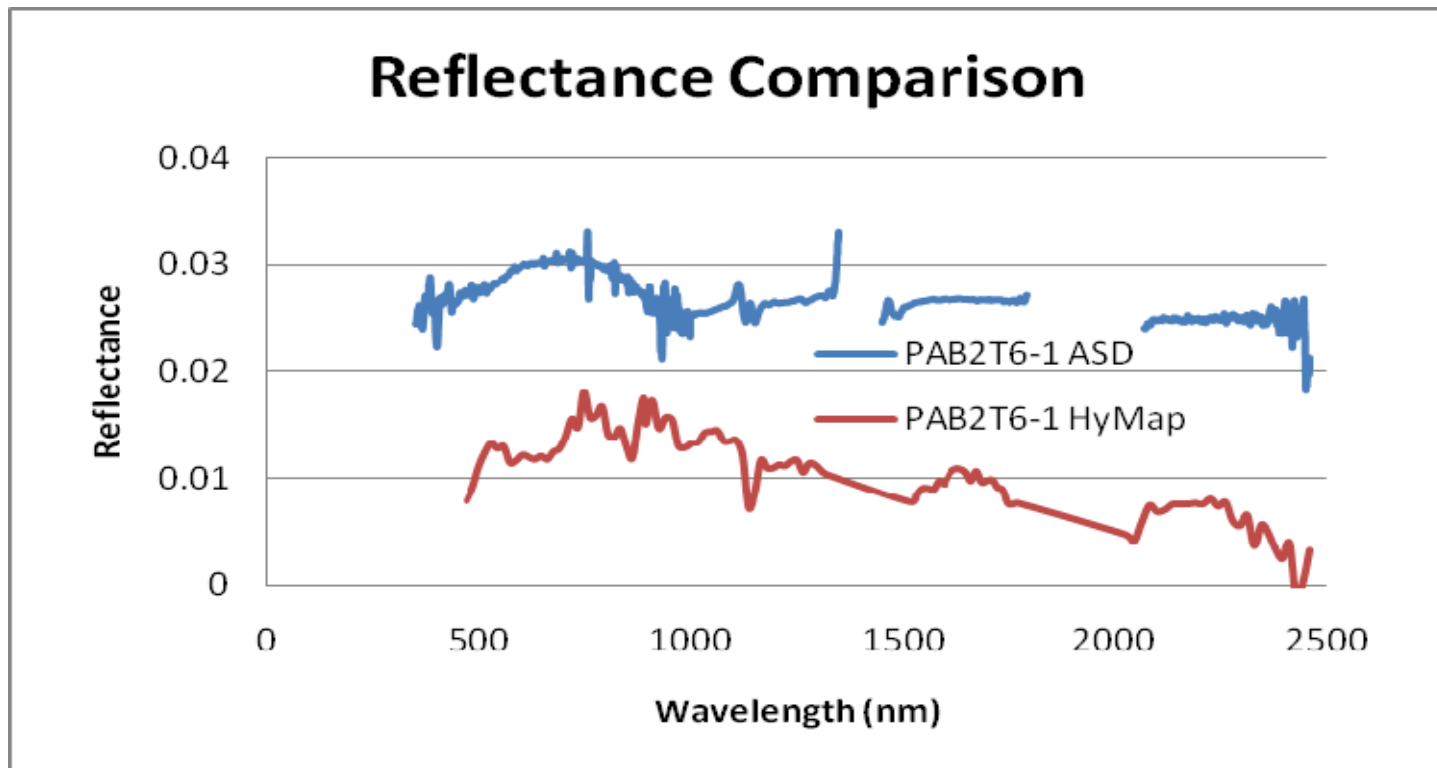Figure 37.   PAB2T6-5 Spectral Comparison

Figure 38.   PAB2T6-1 Spectral Comparison

In the two examples above, it does not appear that the difference is due to the variation in the solar illumination due to cloud cover. If that were the case, the reflectance signatures should only vary by magnitude. So, for calibration purposes to illustrate this, a white calibration panel was captured in each pass of the airborne imager in Pagan. The reflectance values collected by the ASD were compared to the reflectance values from the HyMap image. The two signatures can be seen in Figure 39. The two curves appear to be very similar and only vary in magnitude. This type of variation can be attributed to the different lighting conditions at the times each sample was collected. Furthermore, assuming only a magnitude difference was present in the reflectance values; the program used to generate the trafficability maps does not compare magnitude. It compares angles so this should not lead to non-classification of pixels in the image. The value of the 109 samples in the HyMap image was compared to the ASD values at the same wavelength and an average variation was found to be around 0.43. This factor was applied to the HyMap image and the resulting graph can be seen in Figure 40. The reflectance from the white calibration panel appears to be similar but only varies by magnitude and most likely this variation can be attributed to the variations in the solar illuminations caused by the cloudiness observed at the times each sample was collected.
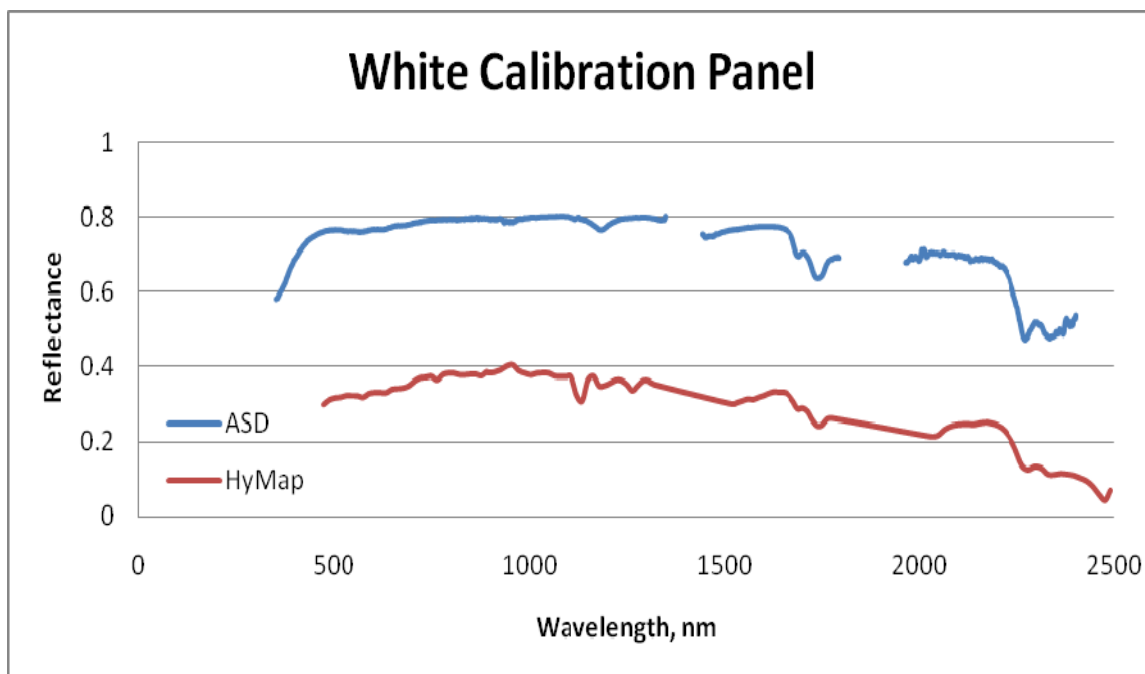
Figure 39.   Reflectance from White Calibraion Panel (Pagan)
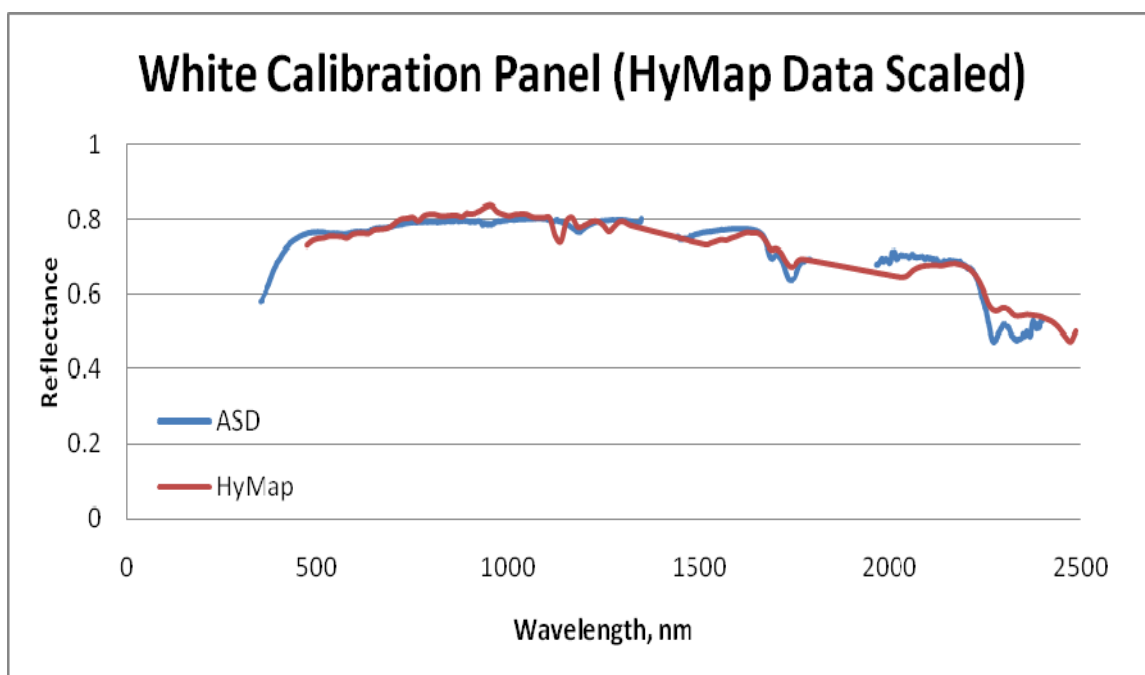

Figure 40.   Reflectance from White Calibration Panel (Pagan, HyMap Data
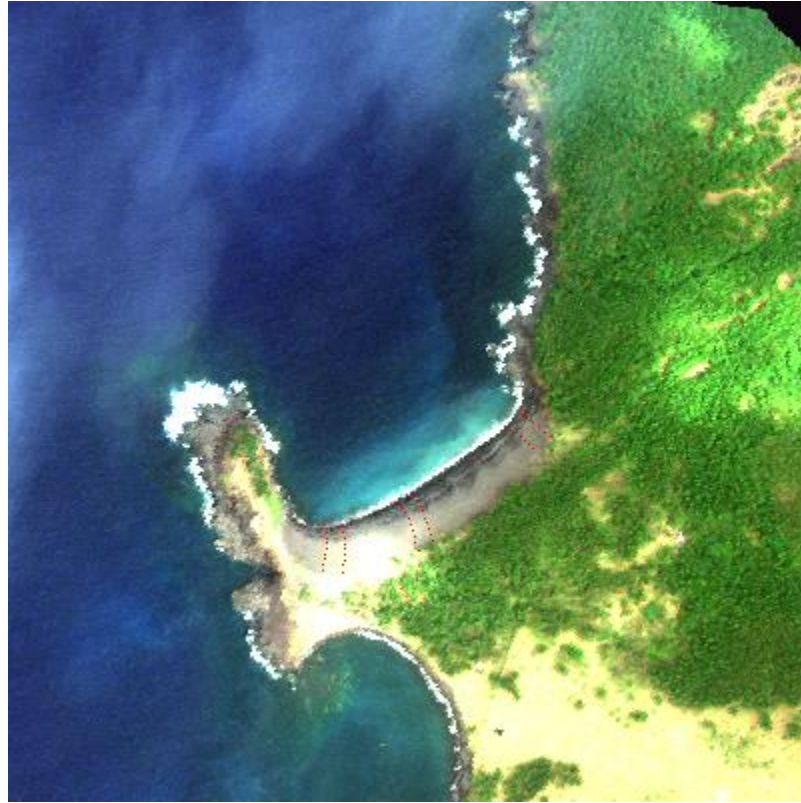Corrected)

59

Figure 41.   Pagan Image with Transect Locations

a.   *Pagan Trafficability Maps*

The SAM is a physically-based spectral classification function in the Environment for Visualizing Images (ENVI) image processing system that uses an n-dimensional angle to match pixels to reference spectra. The algorithm determines the spectral similarity between two spectra by calculating the angle between the spectra, in this case 0.1 radians, and treating them as vectors in a space with dimensionality equal to the number of bands (Research Systems Inc., 2008).

The SAM was used to classify the image using a spectral library containing the spectra from the 52 ground truth points collected from Beach 2 vice the two transects alone that were discussed earlier for ground truth data analysis. Each of the 52 locations has a unique spectral signature, a known deflection modulus, and a known CBR value. Comparing the remaining spectra in the image to a library of spectra with known strength values makes classifying the remaing image relatively simple.

However, to make the images understandable from a trafficability standpoint, the SAM image was color categorized into four colors vice colors for each spectral signature. The four colors were chosen based upon the four categories the USMC has specified in their Reconnaissance Reports Guide Beach Survey Report (BEACHREP) guidance. Green represents regions where trafficability is sufficient for any vehicles, tracked or open-wheeled, and red regions represent areas that would offer significant difficulties in trafficability. Mission commanders would then be able to use this image when choosing a suitable beachfront to land. As per the BEACHREP, trafficability codes range from firm to very soft and will correspond to colors as follows:

Firm(W) = Green

Moderate(X) = Blue

Soft(Y) = Yellow

Very Soft(Z) = Red

Unclassified = Black

A couple of choices were available for how to take the measurements and correlate the measurements to colors. One option assigns a color based upon the CBR percentage. This approach is valid and has proven successful in previous experiments. However, HyMap's resolution is approximately 9m^2. Therefore, the decision was made to not classify the entire pixel area based upon a point measurement. Another option was to use the LWD data gathered from each location. This measurement is a response function to a much larger surface area and therefore, this method was chosen as a valid way to classify each location to assign them a color. The BEACHREP classification will correlate to the Evd trafficability classification as follows:

Trafficability	Evd Value (MN/m^2)	BEACHREP	Color Assignment
Excellent/Good	>21.6	Firm (W)	Green
Fair	14.9 - 21.5	Moderate (X)	Blue
Poor	8.2 - 14.8	Soft (Y)	Yellow
Bad	0 - 8.1	Very Soft (Z)	Red

Table 10.   SAM Color Classification Using Evd Values

The original HyMap image along with the overlaid SAM image from classifying the spectra can be seen in Figure 42.
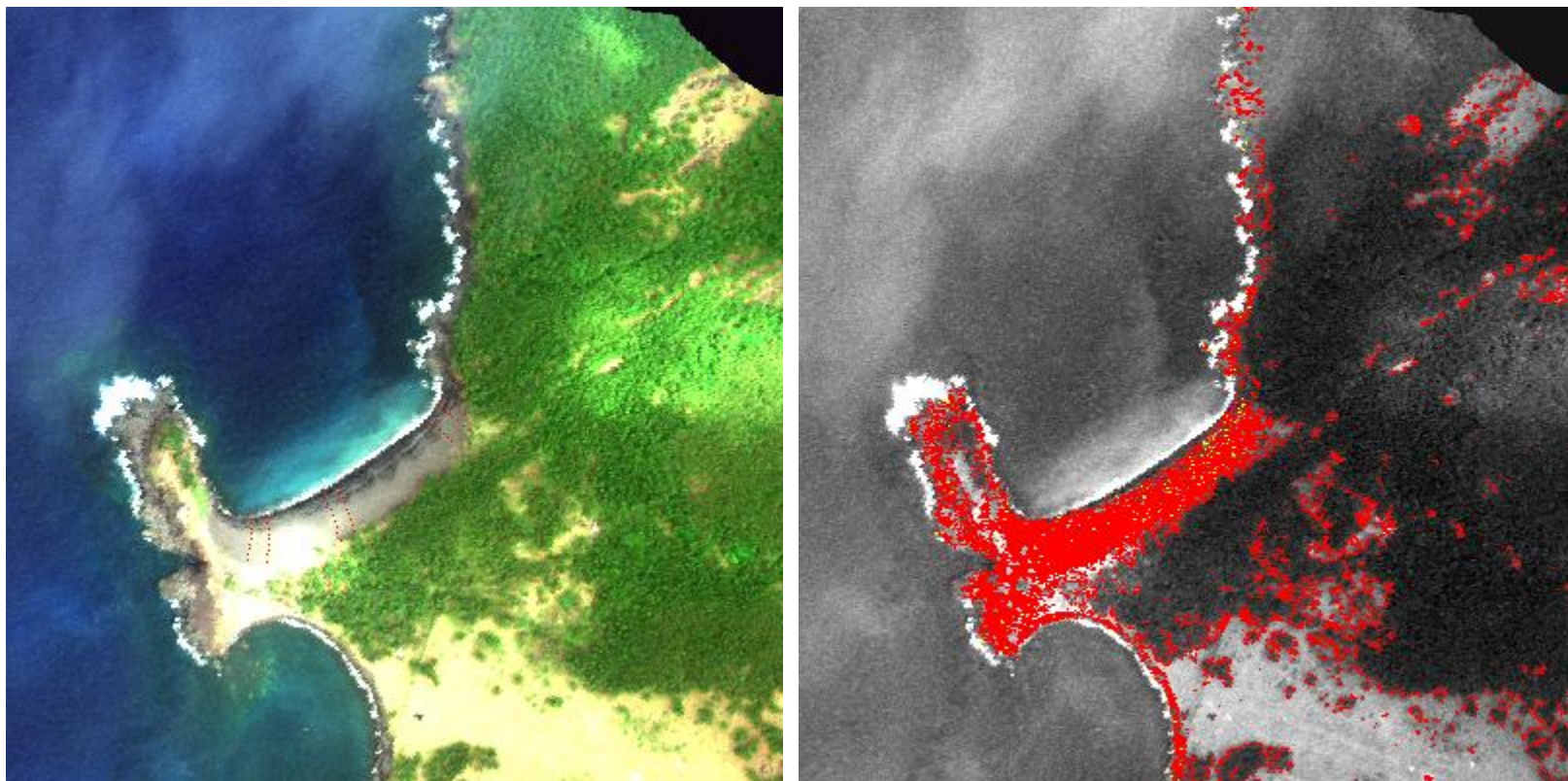

Figure 42.   Pagan HyMap Image and SAM BEACHREP Classification

Based on Figure 37, every location identified with a red pixel can be correlated to a location with similar reflectance data as those identified with having an Evd of less than 8.2MN/m^2. Using Table 10, military planners can see that trafficability throughout Beach 2 is expected to be in the very soft range. There are a few locations that were closely correlated to a soft classification, as can be seen by the yellow pixels. However, the big takeaway for military planners is that Beach 2 in Pagan will present significant difficulties for amphibious landings.

b.   *Tinian Trafficability*

The SAM was used to create the same trafficability maps for Dangkulo Beach in Tinian. Additionally, the same Evd thresholds defined in Table 10were applied to the Tinian image. The original HyMap image along with the overlaid SAM image from classifying the spectra can be seen in Figure 43.
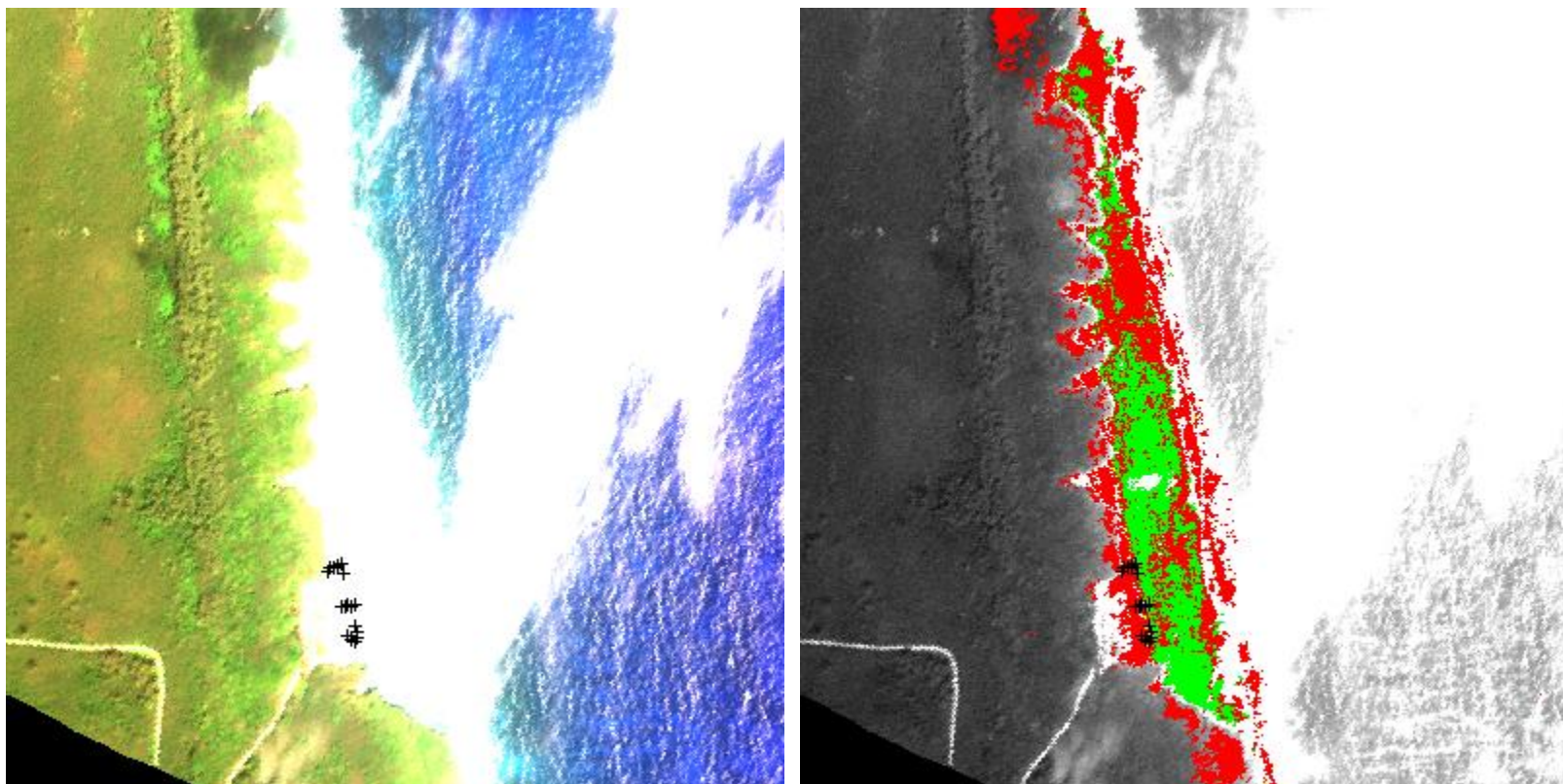
Figure 43.   Tinian HyMap Image and Tinian SAM BEACHREP Classification

By comparing the two SAM images, the littoral regions in Tinian appear to be much more trafficable when compared to Pagan's littoral regions. Knowing the trafficability of the littoral enables military planners to decide which approach lane yields the best chances for success.

C.   STATISTICAL ANALYSIS OF GRAIN SIZES

Something recognized during the analysis of the data was the locations yielding a stronger substrate were the sites having a varied soil grain size distribution. This was discussed in Chapter III and is fundamental to soil engineering. The smaller grain sizes fill in the voids created by the larger grains and creates a stronger substrate. A statistical analysis was performed in efforts to describe this behavior. The values of Variance, Skewness, Kurtosis, and Standard Deviation were calculated and plotted for the locations on Pagan and Tinian that were used in this thesis. An Interactive Data Language (IDL) script was written for this analysis, and the results can be seen in Figure 44. This analysis did not produce the results anticipated. There was not enough variation between the two beaches to sufficiently describe the varied grain size distribution behavior.
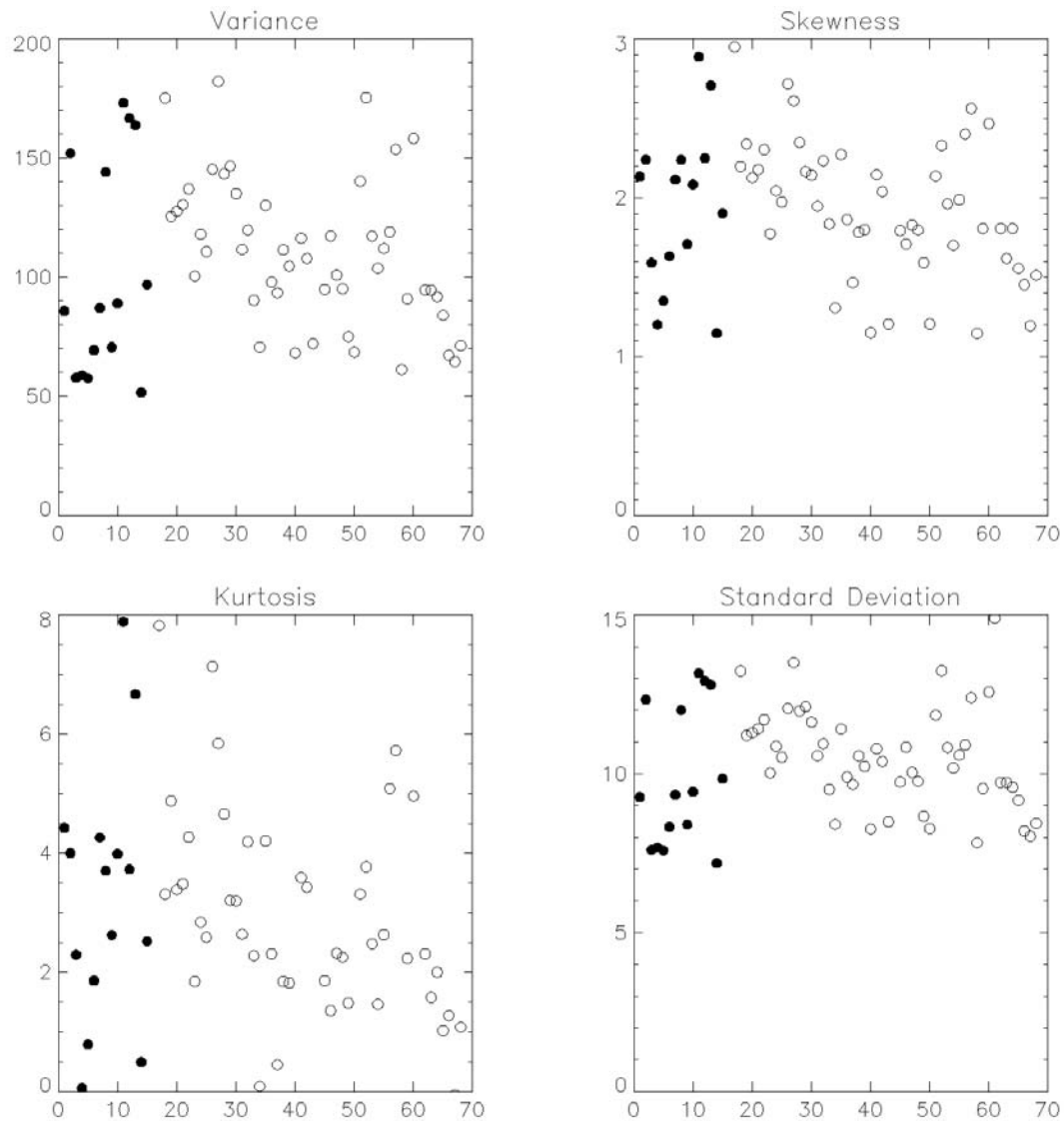
Figure 44.   Statistical Analysis of Grain Size Distribution, Tinian (solid) Pagan (open)

Additionally, the IDL script was used to perform a four term Gaussfit function to the grain size distribution graphs. The first fit was done to the original graphs with the percent of the sample versus the linear value of sieve sizes in microns. Next, the data was modified and the percent of the sample was plotted versus the logs of the sieve sizes. Each method produced similar looking graphs with respect to each other, but they produced different Gaussfit functions to describe them. An example of each graph on a Tinian data point can be seen in Figure 45. Next, the centers were calculated along with

the width of the Gaussfit function on each data location used in this thesis. A plot of each value can be seen in Figure 46, with calculations done using the logarithm of the sieve size.

When analyzing the graphs of the widths and centers, it appears there is something interesting with the groupings of the Pagan data points when compared to the Tinian data points, and when comparing the linear Gaussfit functions to the log Gaussfit functions. To help illustrate this difference, a plot of the Gaussfit center and width values was done with respect to the linear and log scales. The results can be seen in Figure 47 and Figure 48, respectively. It should be noted as well that only a couple of data points from Tinian are not present on Figure 47 and Figure 48, as the focus was to narrow in on the behavior in the lower regions.

Next, the center and width values were correlated to the trafficability to determine if there was a connection. In the Pagan data, nearly every instance when the value of the centers of the Gaussfit was above 1000, this correlated to trafficability values in the red, indicating an Evd value of less than $8.2MN/m^2$. In Tinian, the values above 1000 correlated to trafficability values of red every time. The same correlation was done to the widths and the analysis produced the same conclusion. In nearly every instance in Pagan when the width of the Gaussfit was above 1000, the trafficability value was red and in Tinian, the values above 1000 correlated to trafficability values of red every time. More data should be collected in order to confirm this behavior characteristic but from this limited data set, it appears these values correlate to regions where the trafficability is poor.
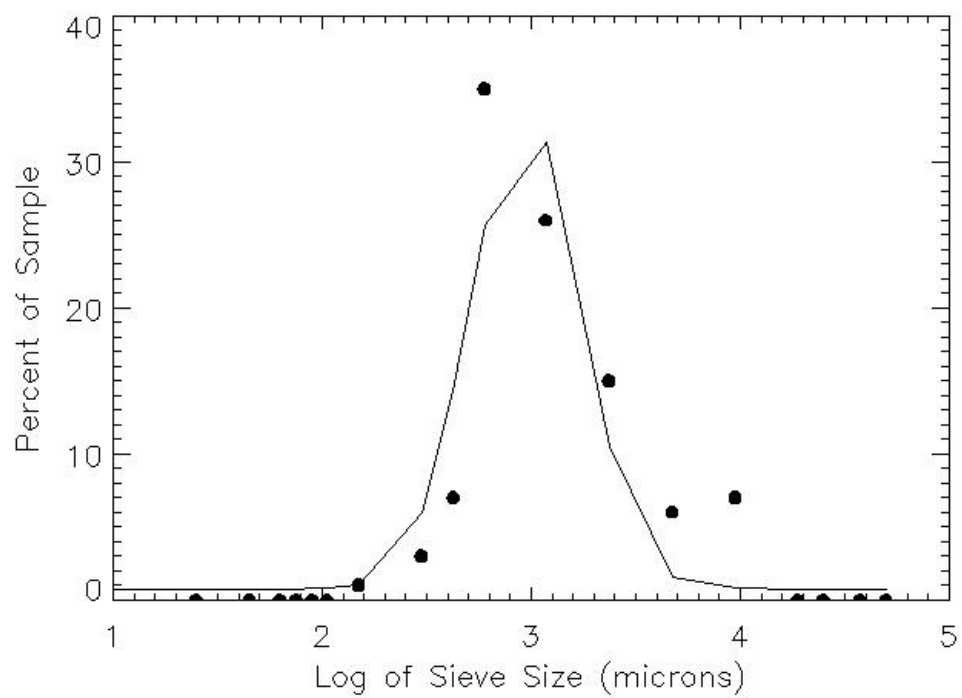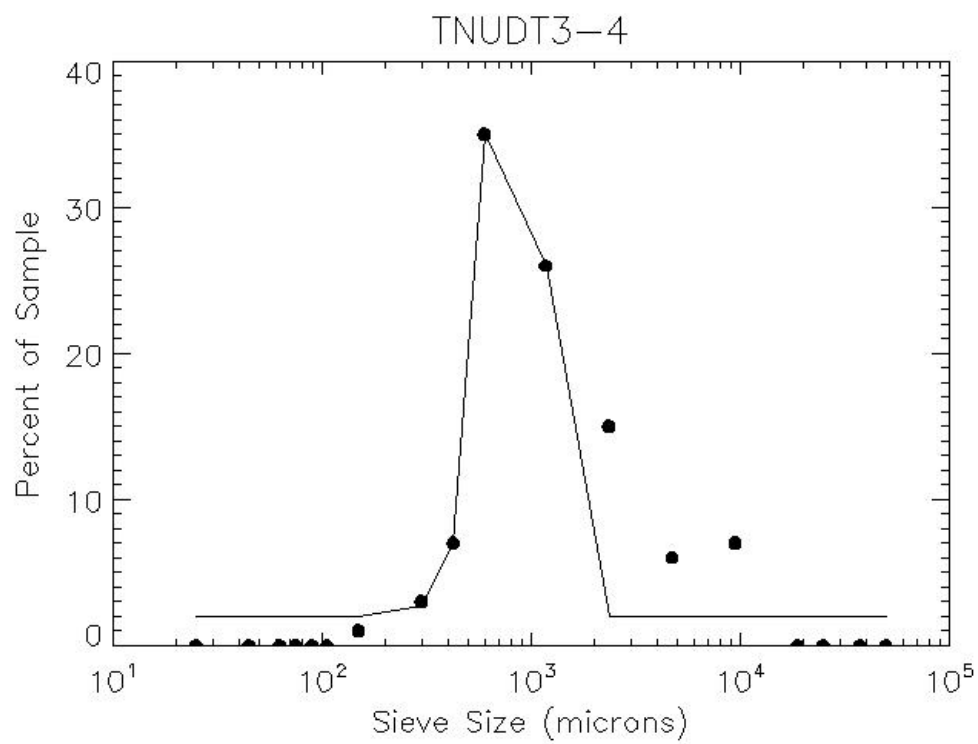
TNUDT3-4

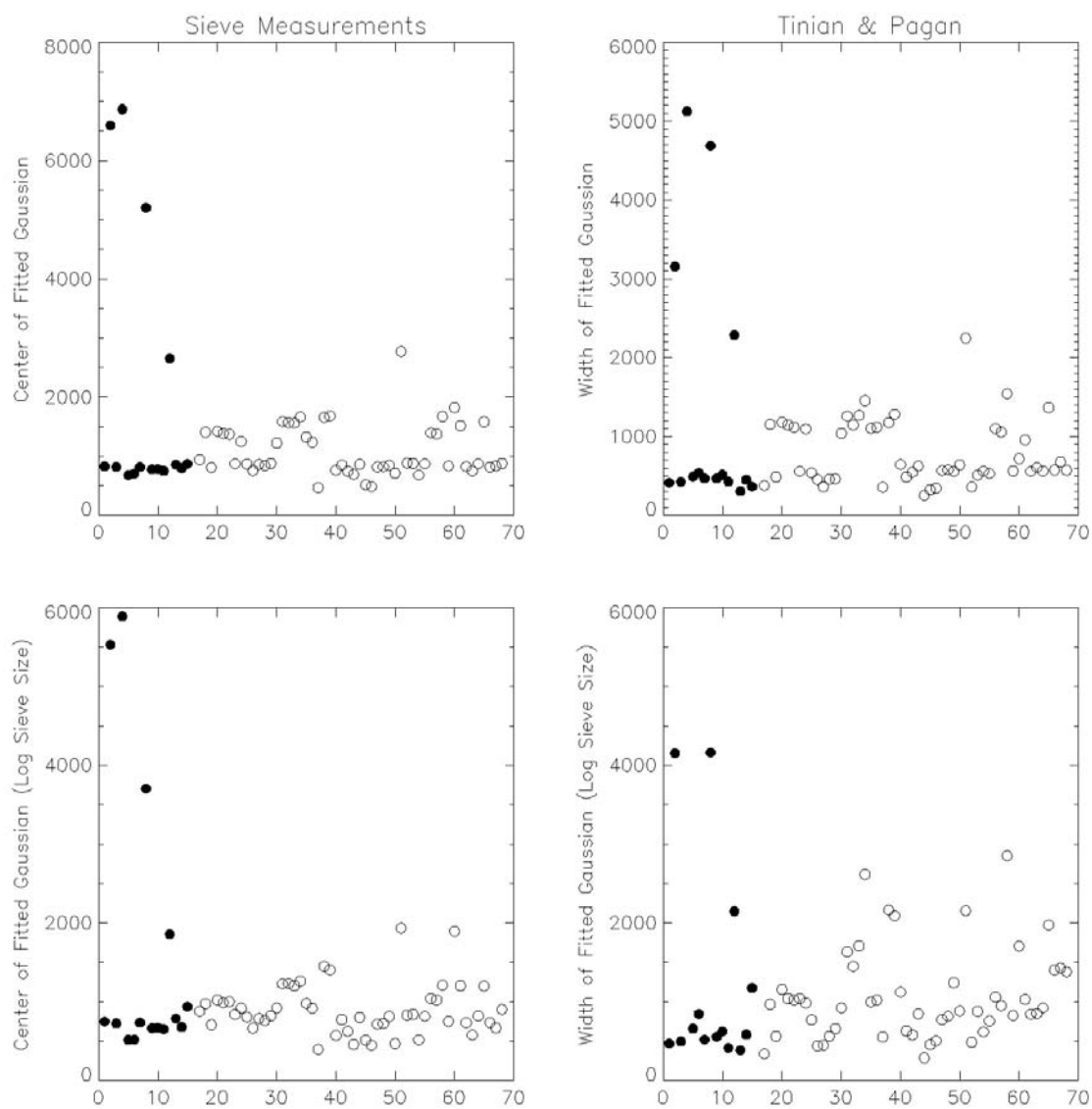Figure 45.   Gaussfit Using IDL

68

Figure 46.   Gaussfit Center and Width Values, Tinian (solid) Pagan (open)
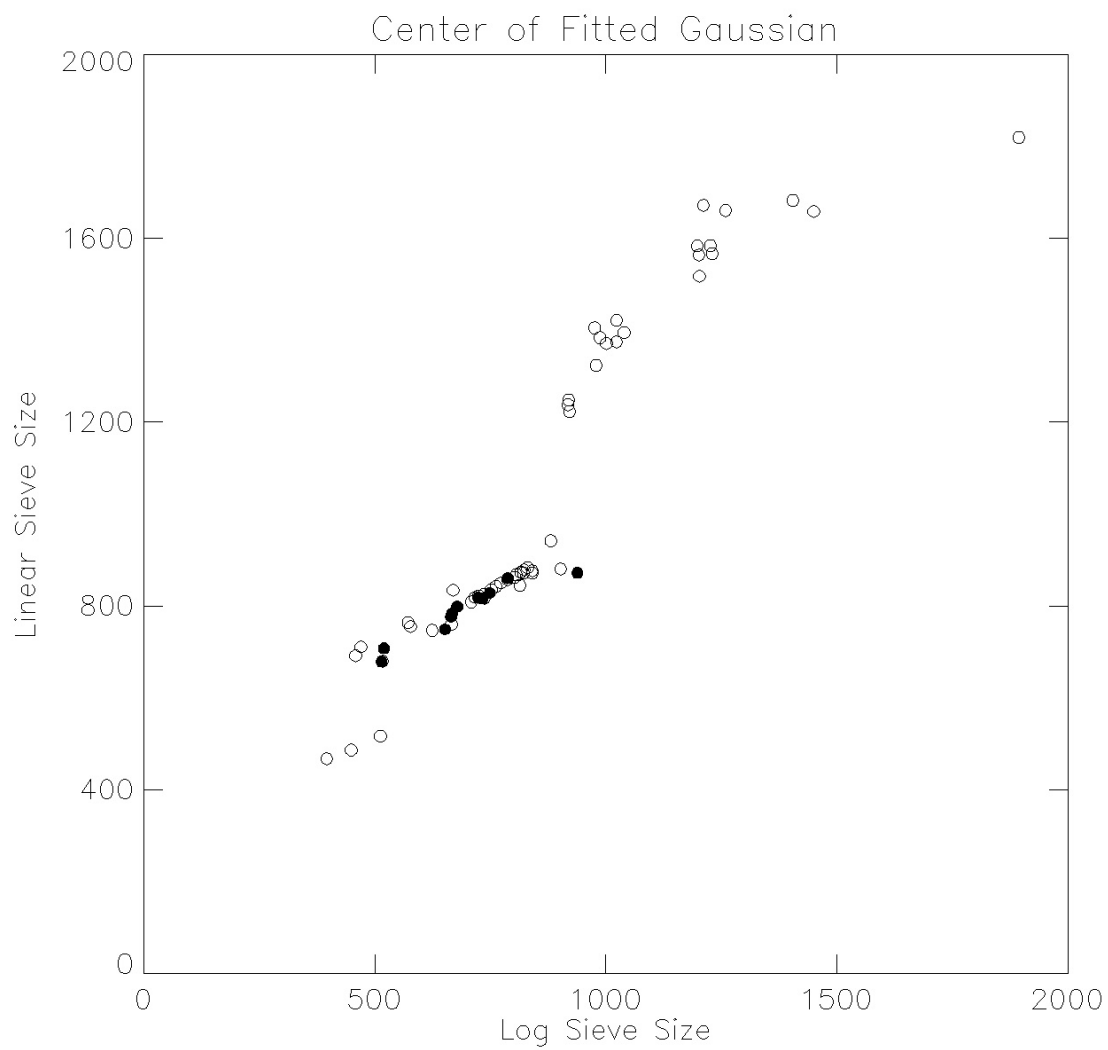
Figure 47.   Gaussfit Center Values, Tinian (solid) Pagan (open)
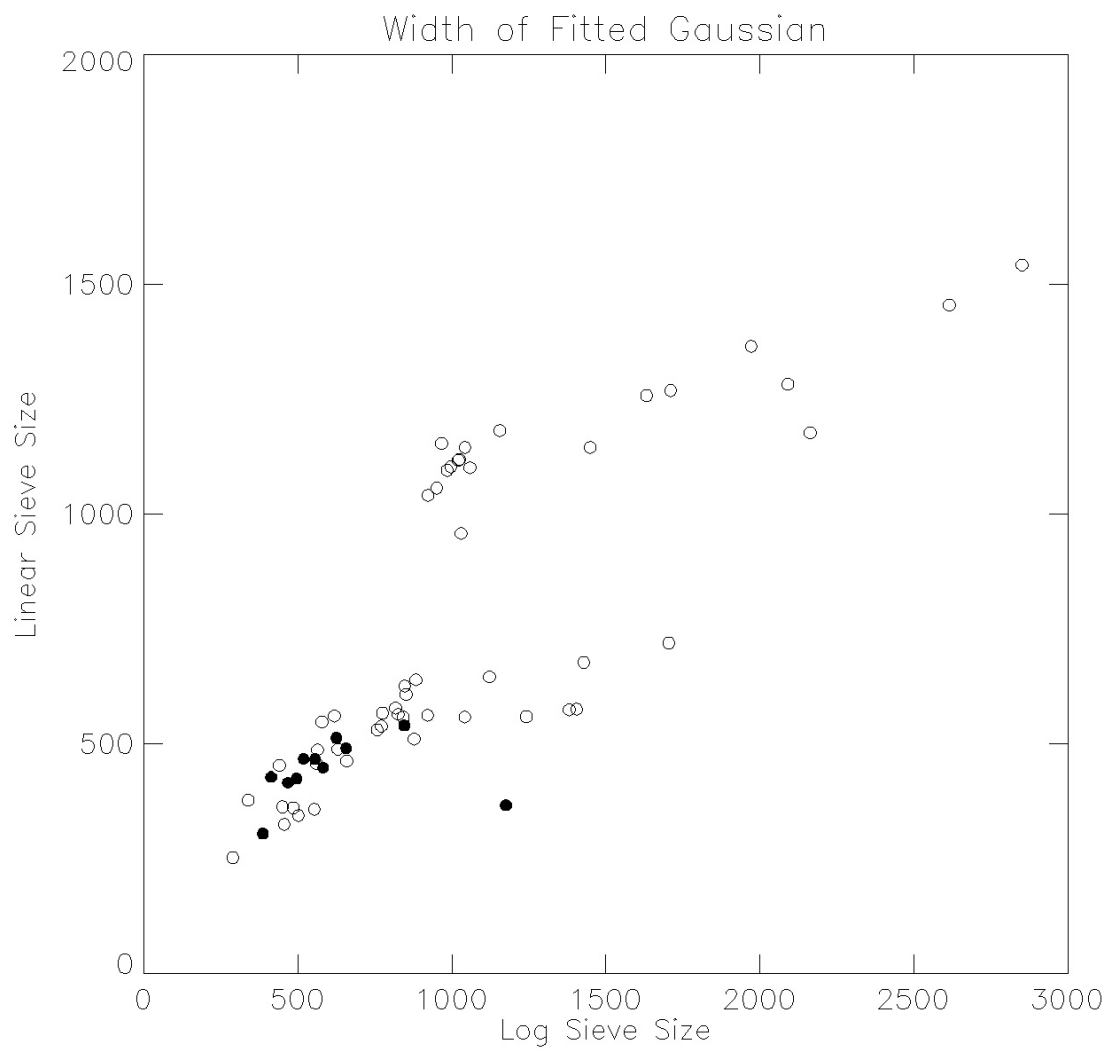
Figure 48.   Gaussfit Width Values, Tinian (solid) Pagan (open)

THIS PAGE INTENTIONALLY LEFT BLANK

VI. CONCLUSIONS AND FUTURE WORK

This thesis has shown that prediction of soil strength in efforts to determine trafficablilty in the littorals is possible from a hyperspectral image. Using the method used in this thesis, initial in situ research is necessary in order to correlate a spectral signature to a measured LWD. The NRL has created a look-up table in which the LWD and DCP values are correlated to a measured spectral signature and this approach has proven successful.

As this thesis illustrated, the littoral region with the stronger substrate was the region containing a varied grain size distribution. However, the first few moments were not enough to properly describe the varied grain size behavior. The Gaussian analysis provided more information indicating a behavior unique to the Pagan data when compared to the Tinian data. Whether this is the data needed to properly describe the grain size distribution remains to be seen but the results show promise and needs further analysis. If a way can be discovered that describes varied grain size distribution behavior that value can be correlated to a hyperspectral signature along with the DCP and LWD data. Ultimately, using a hyperspectral signature alone can produce a table where DCP, LWD, and grain size distribution values can be predicted.

Additionally, the trafficability predictions will improve as the library of spectra is expanded by additional campaigns to gather in situ data. A larger database allows for a finer degree of accuracy for a spectral match when using ENVI's SAM. Using HSI to predict trafficability in the littoral regions is another tool for military planners to use prior to planning amphibious landing in the littorals. Either aircrafts or spacecrafts equipped with this type of technology can deliver the hyperspectral images that the Topographic Platoon-Intelligence Battalion can use when conducting the intelligence preparation of the battlespace.

THIS PAGE INTENTIONALLY LEFT BLANK

LIST OF REFERENCES

Analytical Spectral Devices Representatives. (2002). *FieldSpec Pro User's Guide.* Boulder, CO: Analytical Spectral Devices, Incorporated.

Anderson, R., Malila, W., Maxwell, R., & Reed, L. (1994). *Militarty Utility of Multispectral and Hyperspectral Sensors.* Ann Arbor: Environmental Research Institude of Michigan.

Bachmann, C. M., Montes, M. J., Li, R. R., Woodward, P., Fusina, R., Chen, W., et al. (2008a). *Remote Sensing Retrieval of Substrate Bearing Strength from Hyperspectral Imagery at the Virginia Coast Reserve (VCR'07) Multi-Sensor Campaign.* Boston, MA: Proc. IGARSS'08.

Bachmann, C. M., Montes, M. J., Fusina, R. A., Nichols, R. C., Fry, J. C., Li, R. R., et al. (2010). A Practical Dual-Spectrometer Approach to Measuring In Situ Spectral Reflectance Under Adverse Sky Conditions. *Optics Express*.

Bachmann, C. M., Nichols, C. R., Montes, M., R. Li, P. W., Fusina, R. A., Chen, W., et al. (2010). Retrieval of Substrate Bearing Strength from Hyperspectral Imagery During the Virginia Coast Reserve (VCR '07) Multi-Sensor Campaign. *Marine Goedesy* (33(2-3)), 101–116.

Bachmann, C. M., Nichols, C. R., Murkami, D., & Robert, T. (2010). *Commonwealth of the Northern Mariana Islands Remote Sensing and Field Calibration Validation Campaign 2010 (CNMI'10)*: Science Plan. Washington D.C.: Naval Research Laboratory.

Campbell, J. B. (1996). *Introduction to Remote Sensing.* New York, NY: The Guilford Press.

Cocks, T., Jenssen, R., Stewart, A., Wilson, I., & Shields, T. (1998). *The HYMAP Airborne Hyperspectral Sensor: The System, Calibration and Performance.* Zurich, EARSeL, Paris: 1st EARSeL Workshop on Imaging Spectroscopy.

Ghrefat, H. A., Goodell, P. C., Hubbard, B. E., Langford, R. P., & Aldrouri, R. E. (2007). Modeling grain size variations of aeolian gypsum deposits at White Sands, New Mexico, using AVRIS imagery. *Geomorphology , Vol 88* (Issue 1-2), 57–68.

Goetz, A. F., & Rowan, L. C. (1981). *Geologic Remote Sensing.* Pasadena, CA: American Association for the Advancement of Science.

Kessler, K. C. (2007). *Kessler DCP: Dynamic Cone Penetrometer, K-100 User's Manual and Diskette.* Springfield, VA: Kessler Soils Engineering Products, Inc.

Marine Corps, U. S. (2009). *Amphibious Operations in the 21st Century.* Marine Corps Combat Development Command.

Mitchell, J. K. (1976). *Fundamentals of Soil Behavior.* University of California, Berkeley: John Wiley & Sons, Inc.

Montes, M. J., & Davis, C. O. (2004). *NRL Atmospheric Correction Algorithms for Oceans: Tafkaa User's Guide.* Washington D.C.: Naval Research Laboratory.

Muench, S. T., Mahoney, J. P., & Pierce, L. M. (n.d.). *Washington State Department of Transportation*. Retrieved July 7, 2010, from http://training.ce.washington.edu/wsdot/Modules/04_design_parameters/04-2_body.htm

Navy, DoD. (2000). *Marine Corps Warfare Publication 2-12.1: Geographical Intelligence.* Washington D.C.: Marine Corps.

Olsen, R. C. (2007). *Remote Sensing from Air and Space.* Bellingham, WA: SPIE--The International Society for Optical Engineering.

Spangler, M. G. (1960). *Soil Engineering.* Scranton, PA: The Haddon Craftsmen, Inc.

Tilling, A. K., O'Leary, G. O., Ferwerda, J. G., Jones, S. D., Fitzgerald, G., & Belford, R. (2006). *Remote Sensing to Detect Nitrogen and Water Stress in Wheat.* Melbourne: RMIT University.

Transportation, M. D. (2005). *User's Guide to the Dynamic Cone Penetrometer.* Stendal, Germany: Gerhard ZZorn Mechanische Werkstatten.

INITIAL DISTRIBUTION LIST

1. Defense Technical Information Center
   Ft. Belvoir, Virginia

2. Dudley Knox Library
   Naval Postgraduate School
   Monterey, California

3. R. C. Olsen
   Naval Postgraduate School
   Monterey, California

4. Marine Corps Representative
   Naval Postgraduate School
   Monterey, California

5. Director, Training and Education
   MCCDC, Code C46
   Quantico, Virginia

6. Director, Marine Corps Research Center
   MCCDC, Code C40RC
   Quantico, Virginia

7. Marine Corps Tactical Systems Support Activity
   (Attn: Operations Officer)j
   Camp Pendleton, California